CHAPTER III

PROPERTIES OF THE ROTATING FLUID

A discussion of the behavior of liquid mercury in a rotating liquid mirror system is conducted. For the idealized inviscid fluid, global surface perturbations due to the spherical rotating earth and rotational axis misalignment are addressed as well as the effects of wind or convection induced angular velocity variations. The theoretical and empirical properties of surface waves are described in detail.

A. The Spherical Rotating Earth as a Liquid Mirror Platform

1) Zeroth Order Configuration –

It is serendipitous that the equilibrium configuration of a fluid rotating at constant angular velocity (w), whose axis is parallel to a uniform gravitational field (F_g), is a parabola. The confluence of the centrifugal pseudo-force (F_c) and gravity yield force balance only when the fluid normal vector is perpendicular to a parabolic surface. This arises simply by the monotonic dependence on mirror radial position (r) of the centrifugal force. As derived in Chapter I, the height (z) of the fluid surface as a function of radial position is given by:

$$z = \frac{w^2 r^2}{2g} \qquad \text{(III.A.1a)}$$

This can be written in the form:

$$z = \frac{r^2}{4F} \qquad \text{(III.A.1b)}$$

which we recognize as the equation for a parabola with focal length:

$$F = \frac{g}{2w^2} \qquad \text{(III.A.1c)}$$

where g is the local gravitational acceleration. (g=981.67 cm/s^2 at NODO).

To zeroth order this describes the figure of the LMT primary mirror.

2) Curvature of the Earth –

In the above equation we have neglected the fact the F_g is a radial vector pointing at earth's center. Thus F_g is not everywhere perpendicular to the mirror's surface, but has a radial component pointing inward toward the axis of rotation, whose magnitude is proportional to the radial displacement from the mirror's axis of rotation. The equipotential surface has been given to fourth order in r by Hickson (PC):

$$z = \frac{w^2 r^2}{2g} - \frac{r^2}{2R_E} + \frac{w^2 r^4}{4gR_E^2} + \frac{w^4 r^4}{4g^2 R_E} - \frac{r^4}{8R^3{}_E} \qquad \text{(III.A.2a)}$$

where $R_E = 6.378 \times 10^8$ cm is the Earth's radius.

Factoring out the zeroth order term from those with quadrature dependence on r we have:

$$z = \frac{w^2 r^2}{2g}\left(1 - \frac{g}{R_E w^2}\right) + r^4\left(\frac{w^4}{4g^2 R_E} + \frac{w^2}{4gR_E^2} - \frac{1}{8R_E{}^3}\right) \qquad \text{(III.A.2b)}$$

The corrected focal length F can be written:

$$F = F_0\left(1 - \frac{g}{R_E w^2}\right)^{-1} \qquad \text{(III.A.2c)}$$

Where $F_0 = \frac{g}{2w^2}$ is the zeroth order focal length.

The first order correction in equation (III.A.2a) introduces a correction to the zeroth order focal length that is linearly dependent on focal length itself as seen in equation (III.A.2c). For the NASA-LMT and its 4.51 meter primary mirror focal length, the correction is 1.42 parts per million (ppm) or 6.38 microns (um) which is negligible. Even for a long focal length (30m f/1.5) LMT the large focal shift (0.635 millimeters (mm)) can be easily compensated with a focus adjustment.

The second order correction in equation (III.A.2a) is independent of mirror azimuth and proportional to r^4. This is the first Seidel wave front aberration – spherical aberration. It is small relative to the wave front errors of several waves (λ =500 nanometer (nm) visible green light) induced by atmospheric turbulence (Fried 1966). The surface deviation is only $\Delta z < \lambda/2$ at the perimeter of a 30m diameter f/1.5 LMT. The results of all corrections attributable to the earth's curvature for various LMTs if located at NODO are shown in Table III.A.2-1.

Table III.A.2-1 Various LMTs - Surface Deviations resulting from Earth's Curvature

	F_0 (Term 1) (Zeroth Order Focal length)	1st Order (Term 2) (Focal shift)	2nd Order (Term 3) (Spherical Aberration; Maximum Surface Deviation at mirror perimeter)
NASA-LMT 3.0 m f/1.5037 (w=1.043107)	4.51105 m	+6.38 um (1.42 ppm)	$+4.88\lambda/1{,}000$ (2.44 *nm*)
LZT 6.0 m f/1.5 (w=0.738493)	9.0 m	+25.4 um (2.82 ppm)	$+1.96\lambda/100$ (9.80*nm*)
12.0 m f/1.5 (w=0.522194)	18.0 m	+102 um (5.64 ppm)	$+7.83\lambda/100$ (39.2 *nm*)
20.0 m f/1.5 (w=0.404489)	30.0 m	+282 um (9.41 ppm)	$+2.18\lambda/10$ (108.9*nm*)
30.0 m f/1.5 (w=0.330264)	45.0 m	+635 um (14.1 ppm)	$+4.90\lambda/10$ (245*nm*)

3) Rotation of the Earth –

The Coriolis force associated with the Earth's rotation is a more serious problem than the radial nature of F_g. Coriolis forces introduce a focal shift, coma, astigmatism, and field curvature. Gibson's derivation (Gibson 1990), which neglects the earth's curvature, contains a mistake in the calculation of the vector products. Retaining Gibson's assumptions, but correcting the errors, the equipotential surface to second order is given by:

$$z = \frac{w^2 r^2}{2g} + \frac{w\Omega r^2 \sin\alpha}{g} + \frac{2w^3\Omega r^3 \cos\alpha\cos\beta}{3g^2} + \frac{4w^2\Omega^2 r^3 \sin\alpha\cos\alpha\cos\beta}{3g^2} + \frac{w^4\Omega^2 r^4 \cos^2\alpha\cos^2\beta}{g^3} + \frac{2w^3\Omega^3 r^4 \sin\alpha\cos^2\alpha\cos^2\beta}{g^3} \qquad \text{(III.A.3a)}$$

Where $\Omega = 7.27x10^{-5}$ rad/sec is the Earth's angular rotational velocity, α is the latitude of the mirror, and β is the azimuthal location on the mirror (relative to north) of an arbitrary point. We recover equation (III.A.1a) as $\Omega \to 0$. We also recover equation (III.A.1a) to first order with the substitution $w \to (w + \Omega)$ when $\alpha \to \pm 90$ (for a mirror located at either pole where Coriolis forces only add or subtract to the angular rotational velocity of the mirror and induce only a small focal length shift).

Factoring out the zeroth order term from those with higher order dependence on r we have:

$$z = \frac{w^2 r^2}{2g}\left(1 + \frac{2\Omega \sin\alpha}{w}\right) + \frac{2w^3 \Omega r^3 \cos\alpha \cos\beta}{3g^2} + \frac{4w^2 \Omega^2 r^3 \sin\alpha \cos\alpha \cos\beta}{3g^2} + \frac{w^4 \Omega^2 r^4 \cos^2\alpha \cos^2\beta}{g^3} + \frac{2w^3 \Omega^3 r^4 \sin\alpha \cos^2\alpha \cos^2\beta}{g^3} \quad \text{(III.A.3b)}$$

The corrected focal length F becomes:

$$F = F_0\left(1 + \frac{2\Omega \sin\alpha}{w}\right)^{-1} \quad \text{(III.A.3c)}$$

The first corrective term in equation (III.A.3a) introduces a focal shift as shown in equation (III.A.3c). For the 4.51 m focal length NASA-LMT at the NODO location (α =32.979408 N degree latitude) the shift amounts to 76 ppm or –342 um and is easily compensated by focus adjustments.

The second and third corrective terms in equation (III.A.3a) depend on radial and azimuthal mirror position in the form $r^3 \cos\beta$ corresponding to the second Seidel wave front aberration – coma. For the NASA-LMT at NODO the first coma term introduces a maximum $\pm 3.23\lambda$ ($\pm$ 1.62 micron (um)) surface deviation for the mirror perimeter (at β =0 and 180 degrees for positive and negative deviations respectively) while the second coma term is always negligible ($< \lambda/1000$). Table III.A.3-1 shows maximum surface deviations for the NASA-LMT at various radial and azimuthal mirror positions for the dominant corrective term. Approximately two-thirds of the mirror's surface is subject to surface deviations greater than $\pm \lambda/2$ ($\pm$ 0.250 um) and almost one-third of the

Table III.A.3-1. NASA-LMT: Surface Deviation from 2nd Order Coma Term (Coriolis)

	β =0(+) and 180(-) degrees	$\beta = \pm 30$(+) and ± 150(-) degrees	$\beta = \pm 45$(+) and ± 135(-) degrees	$\beta = \pm 60$(+) and ± 120(-) degrees	$\beta = \pm 90$ deg
Edge Zone (100% area) (r=150 cm)	± 1.62 um $\pm 3.23\lambda$	± 1.40 um $\pm 2.80\lambda$	± 1.14 um $\pm 2.28\lambda$	± 0.81 um $\pm 1.62\lambda$	0
80% Zone (64% area) (r=120 cm)	± 0.827 um $\pm 1.65\lambda$	± 0.716 um $\pm 1.43\lambda$	± 0.585 um $\pm 1.17\lambda$	± 0.414 um $\pm 0.827\lambda$	0
60% Zone (36% area) (r=90 cm)	± 0.349 um $\pm 0.698\lambda$	± 0.302 um $\pm 0.604\lambda$	± 0.247 um $\pm 0.494\lambda$	± 0.174 um $\pm 0.349\lambda$	0
40% Zone (16% area) (r=60 cm)	± 0.103 um $\pm 0.207\lambda$	± 0.090 um $\pm 0.179\lambda$	± 0.073 um $\pm 0.146\lambda$	± 0.052 um $\pm 0.103\lambda$	0
20% Zone (4 % area) (r=30 cm)	± 0.0129um $\pm 0.0259\lambda$	± 0.0112um $\pm 0.0224\lambda$	± 0.0091um $\pm 0.0183\lambda$	± 0.007um $\pm 0.0129\lambda$	0
Center Zone (r=0 cm)	0	0	0	0	0

surface has deviations greater than $\pm\lambda$. Ideally these errors should be compensated in the corrective optics, but the additional complexity would have been cost prohibitive. Image degradation resulting from deviations at this level will be masked by mirror speed variations (Section III.D) and observatory (dome) and atmospheric seeing and have minimal effect. For larger LMTs, however, the surface deviations can reach >100 λ (30 m f/1.5 LMT) and should be compensated in the corrective optics. Interestingly, the Coriolis induced coma occurs axially as well as off-axis, unlike the purely off-axis coma normally associated with parabolic mirrors and already compensated in the original 3-element and present 4-element NASA-LMT corrector.

The fourth and fifth corrective terms in equation (III.A.3a) are proportional to both radial and azimuthal mirror position in the form $r^4 \cos^2 \beta$ which is a combination of the third and fourth Seidel wave front aberrations – astigmatism and field curvature. The corrections depend on both radial and azimuthal mirror position. These terms are negligible for the NASA-LMT ($< \lambda$/10,000) as well as for a much larger 30 m f/1.5 LMT ($< \lambda$/200). The maximum results of all corrections attributable to the earth's rotation for various LMTs if located at NODO are shown in Table III.A.3-2.

B. Axial Tilt

Ideally, the rotational axis of the mirror should be parallel to Fg. In reality, the mechanics of the supporting structure and the errors in the instrumentation used to determine level, set a limit to the degree to which true parallelism can be attained.

Table III.A.3-2. Various LMTs - Surface Deviations resulting from Coriolis Effects

	1st Order (Term 2) (Focal shift)	2nd Order (Term 3 & 4) (Coma; Maximum Surface Deviation - mirror perimeter at β = 0(+) and 180(-) degrees)		3rd Order (Term 5 & 6) (Astigmatism and Field Curvature; Maximum Surface Deviation – mirror perimeter at β = 0 or 180 degrees)	
NASA-LMT 3.0 m f/1.5037 (w=1.043107)	-342 um (76 ppm)	$\pm$ 1.62 um $\pm 3.23\lambda$	$\pm$ 0.123 nm $\pm \frac{0.245\lambda}{1000}$	+0.0236 nm $+\frac{0.047\lambda}{1000}$	+1.79 fm << $\frac{\lambda}{10{,}000{,}000}$
LZT 6.0 m f/1.5 (w=0.738493)	-965 um (107 ppm)	$\pm$ 4.59 um $\pm 9.18\lambda$	$\pm$ 0.492 nm $\pm \frac{0.984\lambda}{1000}$	+0.0947 nm $+\frac{0.189\lambda}{1000}$	+10.2 fm << $\frac{\lambda}{10{,}000{,}000}$
12.0 m f/1.5 (w=0.522194)	2730 um (152 ppm)	$\pm$ 13.0 um $\pm 25.9\lambda$	$\pm$ 1.97 nm $\pm \frac{3.94\lambda}{1000}$	+0.379 nm $+\frac{0.757\lambda}{1000}$	+57.4 fm $+\frac{1.15\lambda}{10{,}000{,}000}$
20.0 m f/1.5 (w=0.404489)	5873 um (196 ppm)	$\pm$ 27.9 um $\pm 55.8\lambda$	$\pm$ 5.47 nm $\pm \frac{1.09\lambda}{100}$	+1.05 nm $+\frac{2.10\lambda}{1000}$	+206 fm $+\frac{4.12\lambda}{10{,}000{,}000}$
30.0 m f/1.5 (w=0.330264)	10790 um (240 ppm)	$\pm$ 51.3um $\pm 103\lambda$	$\pm$ 12.3 nm $\pm \frac{2.46\lambda}{100}$	+2.37 nm $+\frac{4.73\lambda}{1000}$	+568 fm $+\frac{1.14\lambda}{1{,}000{,}000}$

In the case of the NASA-LMT utilizing a 5 arcsecond/division spirit level mounted on the mirror itself (Chapter V), parallelism to approximately ± 0.2 arcsecond can be achieved. An alternative electronic level enables ± 0.04 arcsecond accuracy. Girard and Borra (1997) have suggested that <0.5 arcsecond parallelism error in the laboratory is sufficient to reduce tilt-induced aberrations to acceptable levels for small LMTs . Results obtained with the NASA-LMT are inconclusive. A series of images shown in Chapter V illustrates entrance pupil images obtained at parallelism errors of 0, 1 and 7 arcseconds. Poor atmospheric seeing the night this data was acquired has likely obscured the results, but there is evidence of an intensified annulus in the highly tilted case.

Gibson (1990) has shown analytically the aberrations induced by a lack of parallelism for the case neglecting the earth's curvature. Hickson (PC) has recently performed the analysis without this simplification. The treatment here follows Gibson's and therefore is only approximate in terms of the magnitude of the errors and their classification and as such should be used as a qualitative guide. An exact solution should utilize Hickson's treatment once published.

With minor modification to align β with the direction of axial tilt, the equipotential surface in the plane of the mirror can be represented by (Gibson 1990):

$$z = \frac{w^2 r^2}{2g}\sec\theta + r\tan\theta\cos\beta \qquad \text{(III.B.a)}$$

Where θ is the angle between F_g and the mirror rotational axis, and β is the azimuthal

location on the mirror (relative to the tilted direction) of an arbitrary point. The corrected focal length F becomes:

$$F = F_0(\sec\theta)^{-1} = F_0\cos\theta \qquad \text{(III.B.b)}$$

The first term introduces a simple focal length shift dependent on $\cos\theta$. Even for a 7 arcsecond tilt, the shift amounts to only 1 part per billion (ppb) or 4.5 nm for the NASA-LMT. For larger mirrors, similarly tilted, the shift is small and easily compensated (10 ppb or 450 nm for a 30m f/1.5).

The second term, proportional to r $\cos\beta$, signifies distortion and can be interpreted as an asymmetric thickening of the Hg layer progressing from the high edge of the mirror (β=180 degrees; thinner) to the low end (β=0 degrees; thicker). For the NASA-LMT with a 1 arcsecond tilt error, this term yields a maximum surface deviation at the mirror perimeter of ± 7.27 um or $\pm 14.5\lambda$ (at β=0 and 180 degrees for positive and negative deviations respectively). With a 7 arcsecond tilt error, the maximum surface deviation for the mirror perimeter increases to ± 50.9 um or $\pm 102\lambda$. These are significant perturbations to the mirror's parabolic surface and convey the importance of accurate mirror axial tilt alignment. Ideally the NASA-LMT mirror should be parallel to F_g within 0.1 arcsecond or better in order to bring the maximum surface deviation to $< \pm 1.45\lambda$. At this level, image degradation will be masked by mirror speed variations (Section III.D) and observatory (dome) and atmospheric seeing and have minimal effect.

Compensation must obviously be made by proper axial alignment rather than an arbitrary constraint on the design of corrective optics. Table III.B-1 lists maximum surface deviations (along the β =0-180 degree axis) for a range of tilt errors and mirror radial positions for the NASA-LMT.

Since at a constant axial tilt error the surface deviation increases linearly with mirror radial position at a given mirror azimuth (β), the situation is more serious for larger LMTs. A 30m f/1.5 LMT with 0.1 arcsecond tilt error, will have a maximum surface deviation of ± 7.27 um or $\pm 14.5\lambda$, which is identical to the maximum shown for a 3.0 m NASA-LMT with 1 arcsecond tilt error. Larger LMTs must be more accurately aligned than smaller LMTs for a given surface deviation criteria.

C. Fluid Thermal Expansion

The finite coefficient of expansion for Hg (0.18 um/mm-^oC when constrained in two dimensions; Gibson 1990) implies a small displacement to the focal length due to expansion or contraction of the Hg film itself. During an evening's data acquisition, the temperature of the mirror can vary by as much as 25 ^oC . For the 1.61 mm Hg film thickness incorporated by the NASA-LMT, this yields a 7.25 um change in height of the parabolic surface. This is negligible however relative to the 54 um/^oC focal shift attributable to the mirror container and prime focus structural components (Chapter IV).

Table III.B-1. NASA-LMT: Surface Deviation from Mirror Tilt Distortion Term

	θ = 1.0 arcsecond	θ = 0.5 arcsecond	θ = 0.2 arcsecond	θ = 0.1 arcsecond	θ = 0.01 arcsecond
Edge Zone (100% area) (r=150 cm)	± 7.27 um ± 14.5λ	± 3.63 um ± 7.25λ	± 1.45 um ± 2.90λ	± 0.727 um ± 01.45λ	± 0.0727 um ± 0.145λ
80% Zone (64% area) (r=120 cm)	± 5.82 um ± 11.6λ	± 2.91 um ± 5.80λ	± 1.16 um ± 2.32λ	± 0.582 um ± 1.16λ	± 0.0582 um ± 0.116λ
60% Zone (36% area) (r=90 cm)	± 4.37 um ± 8.7λ	± 2.18 um ± 4.35λ	± 0.873 um ± 1.74λ	± 0.437 um ± 0.87λ	± 0.0437 um ± 0.087λ
40% Zone (16% area) (r=60 cm)	± 2.91um ± 05.8λ	± 1.46 um ± 2.9λ	± 0.583 um ± 1.16λ	± 0.291 um ± 0.58λ	± 0.0291 um ± 0.058λ
20% Zone (4 % area) (r=30 cm)	± 1.46 um ± 2.9λ	± 0.728 um ± 1.45λ	± 0.291 um ± 0.58λ	± 0.146 um ± 0.29λ	± 0.0146 um ± 0.029λ
Center Zone (r=0 cm)	0	0	0	0	0

D. Mirror Angular Velocity Stability

It is straightforward to derive the requisite angular velocity stability of the mirror by assuming Hg is a perfect fluid of zero viscosity and that speed variations translate into focal length (F) variations alone. This ignores the complex effects associated with wave activity and fluid flow driven by small speed changes and the surface deviations and wave front errors that result. In considering focal stability (dF) as it relates to angular velocity (ω), a simple analytic approach yields, by differentiating each side of Equation (III.A.1c), the relation:

$$\frac{dF}{F} = \frac{-2d\omega}{\omega} \qquad \text{(III.D.a)}$$

By the simple geometry of the converging optical beam, the focal instability can be related to a resultant defocusing profile of characteristic size (I):

$$I_{Focus} = 2 \cdot D \cdot \frac{d\omega}{\omega} \qquad \text{or} \qquad I_{Focus} = \frac{dF}{R} \qquad \text{(III.D.b)}$$

where D is the mirror diameter, and R is the effective focal ratio including the corrector (which has weakly positive power) $R = \frac{F}{D} = 1.7189$.

The final image size is given by a convolution of the defocusing profile caused by

the focal variations with the atmospheric seeing profile (Hickson PC). The final image size is given exactly by adding the second moments of these profiles in quadrature, or approximately by using the FWHM:

$$I_{Final}^2 \cong I_{Seeing}^2 + I_{Focus}^2 \qquad \text{(III.D.c)}$$

which using (III.D.b) can be rewritten in terms of angular velocity variation:

$$\frac{d\omega}{\omega} = \frac{I_{Seeing}}{2D}\sqrt{\left(\frac{I_{Final}}{I_{Seeing}}\right)^2 - 1} \qquad \text{(III.D.d)}$$

If we allow angular velocity induced focal variations to yield a 5% expansion of the final image profile relative to the nominal seeing disk:

$$\frac{I_{Final}}{I_{Seeing}} = 1.05 \qquad \text{(III.D.e)}$$

then inserting the nominal value for the minimum seeing at NODO (Smith and Salisbury 1961) of $3.8785x10^{-6}\,rad$ (0.8 arcsecond), equivalent to a profile width of 20 um at the NASA-LMT focal plane, into equation (III.D.d) yields:

$$\frac{d\omega}{\omega} = -1.07x10^{-6} = 1.07 \text{ ppm} \qquad \text{(III.D.f)}$$

Equivalently, in term of mirror period $(P = \frac{2\pi}{\omega})$, we have:

$$\frac{dP}{P} = \frac{-d\omega}{\omega} = 1.07x10^{-6} = 1.07 \text{ ppm} \qquad \text{(III.D.g)}$$

Empirical results relating mirror angular velocity (or mirror period) stability to image quality have been obtained for the first time with the NASA-LMT. Mirror angular velocity data have been recorded under various observing conditions while astronomical data was simultaneously acquired. Figures III.D-1 through 5 show the correlation between mirror angular velocity stability and image quality. The five night's data indicate that mirror angular velocity stability is crucial to obtaining good image quality. As the mirror period error decreases, the image quality improves as quantified by the full-width-half-maximum (FWHM) of the stellar point-spread-functions (PSF). Other factors such as atmospheric seeing complicate the relationship between mirror period error and image quality. Small scale correlations are present but limited, whereas large scale trends are clearly evident in each of the five nights. This is true even in Figure III.D-2 wherein the correlation is evident despite erratic seeing which caused large amplitude oscillations in the FWHM. The confidence in each case exceeds 99% as determined by the correlation coefficient (Taylor 1982) for each night's data.

In each of these five nights, the mirror stability is never better than 4 ppm and is more typically between 5 and 20 ppm while observing. In light of the ~1 ppm stability requirement for a maximum 5% image blur (III.D.g), it is evident that additional performance can be obtained by improving the rotational stability of the mirror. This can be achieved primarily by better control of air currents around the mirror which is located 10 meters from the dome aperture in a recessed enclosure surrounded by a shroud extending 2 meters above and 1 meter below the mirrors surface. Despite this protection, the mirror is still subject to the effects of external winds as well as convective air currents arising from the differential heating and cooling associated with the LMT superstructure and the observatory itself. The installation of wind baffles and sensitive air motion sensors that can detect flows of <20 cm/second are being considered to better monitor and control the mirror environment and thereby improve mirror rotational stability.

As a baseline for mirror angular velocity stability the mirror period has been recorded with the observatory dome closed. Figures III.D-6 through 8 show that even under these quiescent conditions the mirror retains a residual period error of between 1 and 2 ppm due to convection and inaccuracies in the motor drive and electronics. Figure III.D-6 demonstrates the return of the mirror to a quiescent state after the observatory dome is closed (t=0) at the end of an evening's observations. Figures III.D-7 and 8 appear to illustrate the effects of external winds leaking into the dome cavity while the dome is closed. Figure III.D-7 terminates with the dome opening for an evening's observing, demonstrating the characteristic increase in mirror period instability when the mirror is exposed to the external environment.

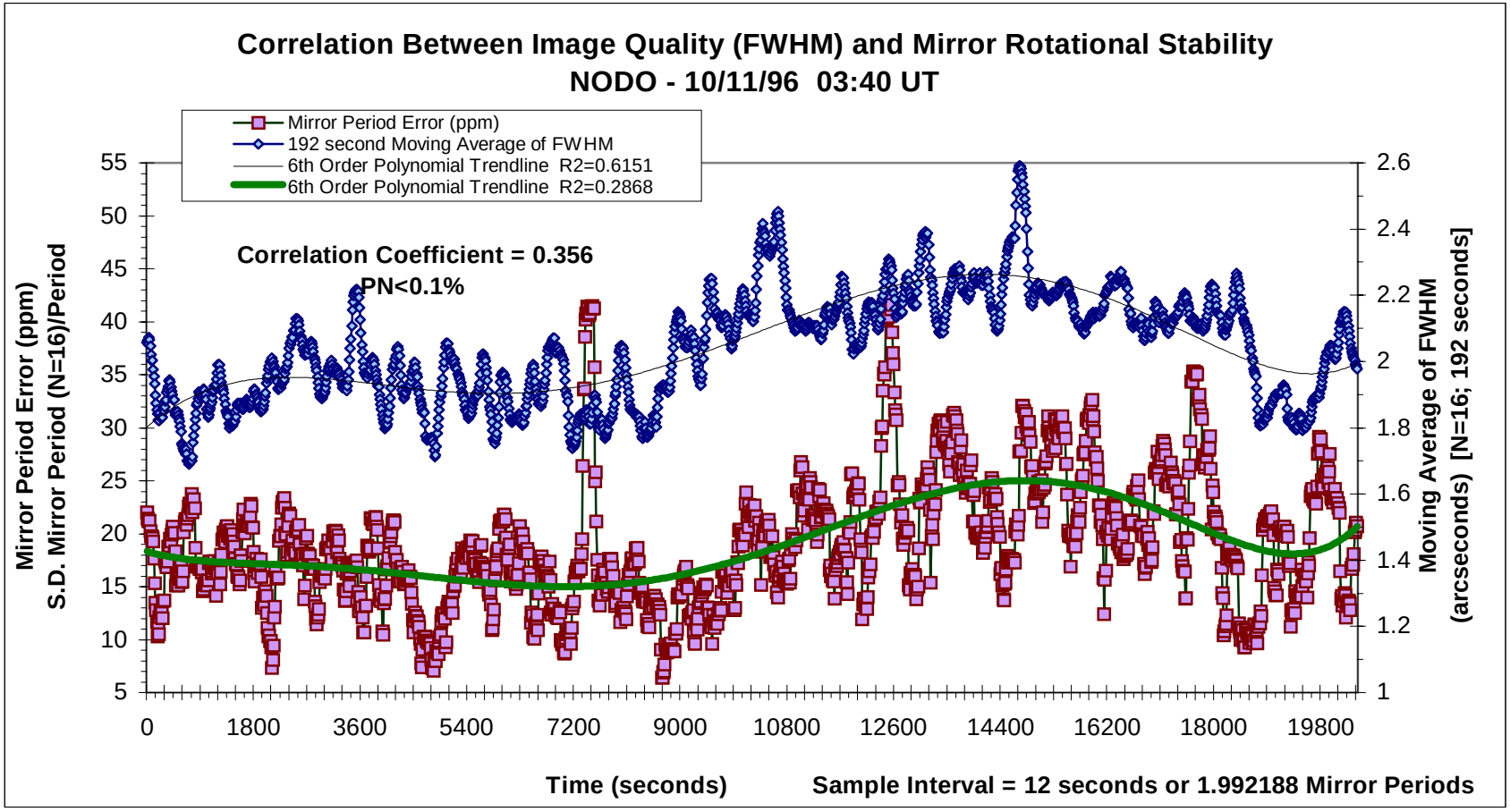

Figure III.D-1. The correlation between instability of the mirror rotational period and image quality. The upper trace (blue) is a 192 second moving average of the FWHM of stellar images taken from a TDI scan acquired while the mirror rotational period was recorded (both at 12 second intervals). The lower trace (pink) is the standard deviation of each 16 samples (192 seconds) of the mirror rotational period normalized by the mean rotational period to yield a relative measure of the mirror rotational instability (ppm). The traces correlate with >99.9% confidence. The correlation is subject to the additional influence of atmospheric seeing. Trendlines are shown only to illustrate the overall correlation.

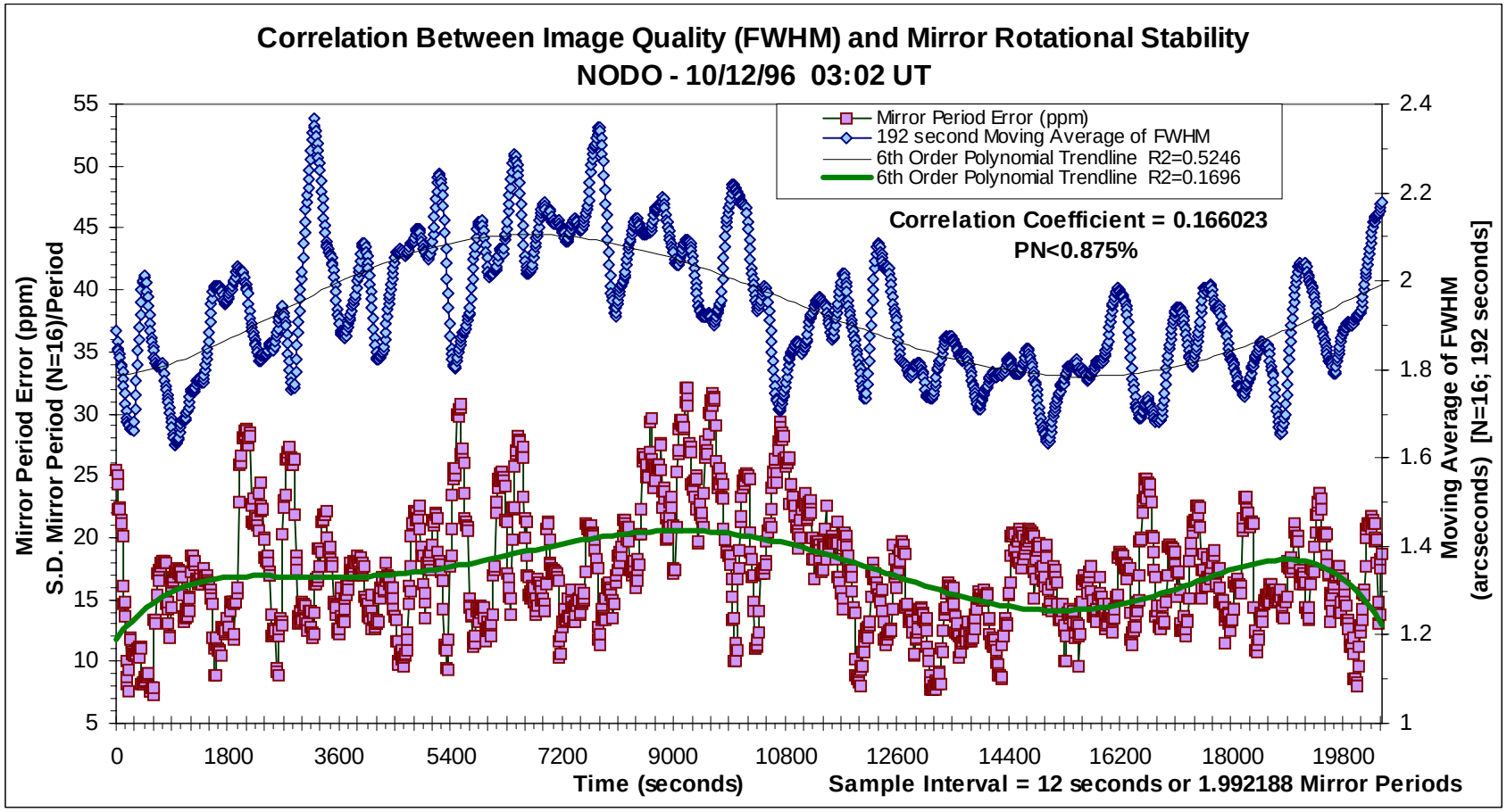

Figure III.D-2. The correlation between instability of the mirror rotational period and image quality. The upper trace (blue) is a 192 second moving average of the FWHM of stellar images taken from a TDI scan acquired while the mirror rotational period was recorded (both at 12 second intervals). The lower trace (pink) is the standard deviation of each 16 samples (192 seconds) of the mirror rotational period normalized by the mean rotational period to yield a relative measure of the mirror rotational instability (ppm). The traces correlate with >99.9% confidence. The correlation is subject to the additional influence of atmospheric seeing (large amplitude oscillations in the FWHM trace).

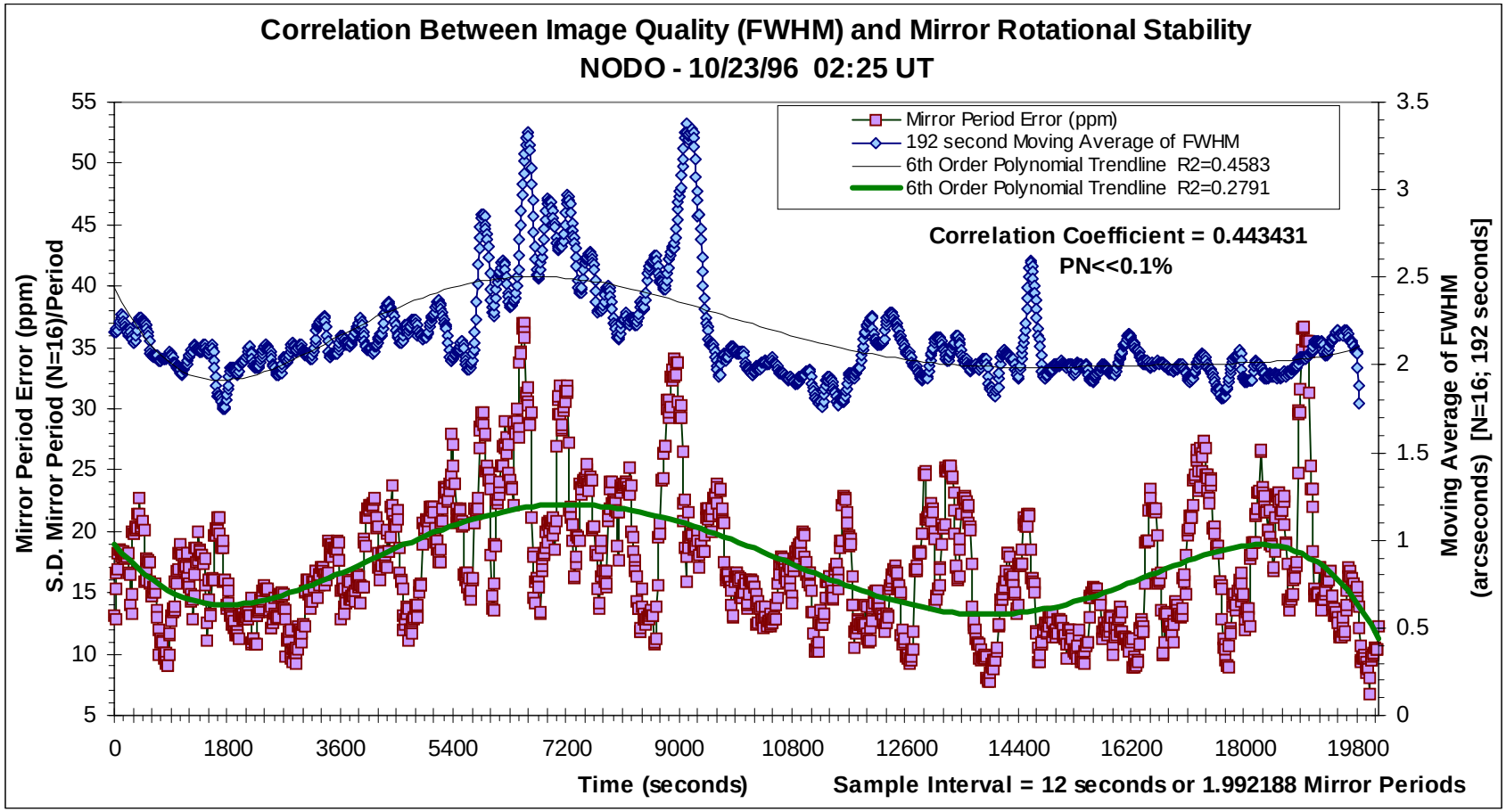

Figure III.D-3. The correlation between instability of the mirror rotational period and image quality. The upper trace (blue) is a 192 second moving average of the FWHM of stellar images taken from a TDI scan acquired while the mirror rotational period was recorded (both at 12 sec intervals). The lower trace (pink) is the standard deviation of each 16 samples (192 seconds) of the mirror rotational period normalized by the mean rotational period to yield a relative measure of the mirror rotational instability (ppm). The traces correlate with >99.9% confidence. The correlation is subject to the additional influence of atmospheric seeing. Several sharp FWHM peaks correlate well with mirror speed anomalies.

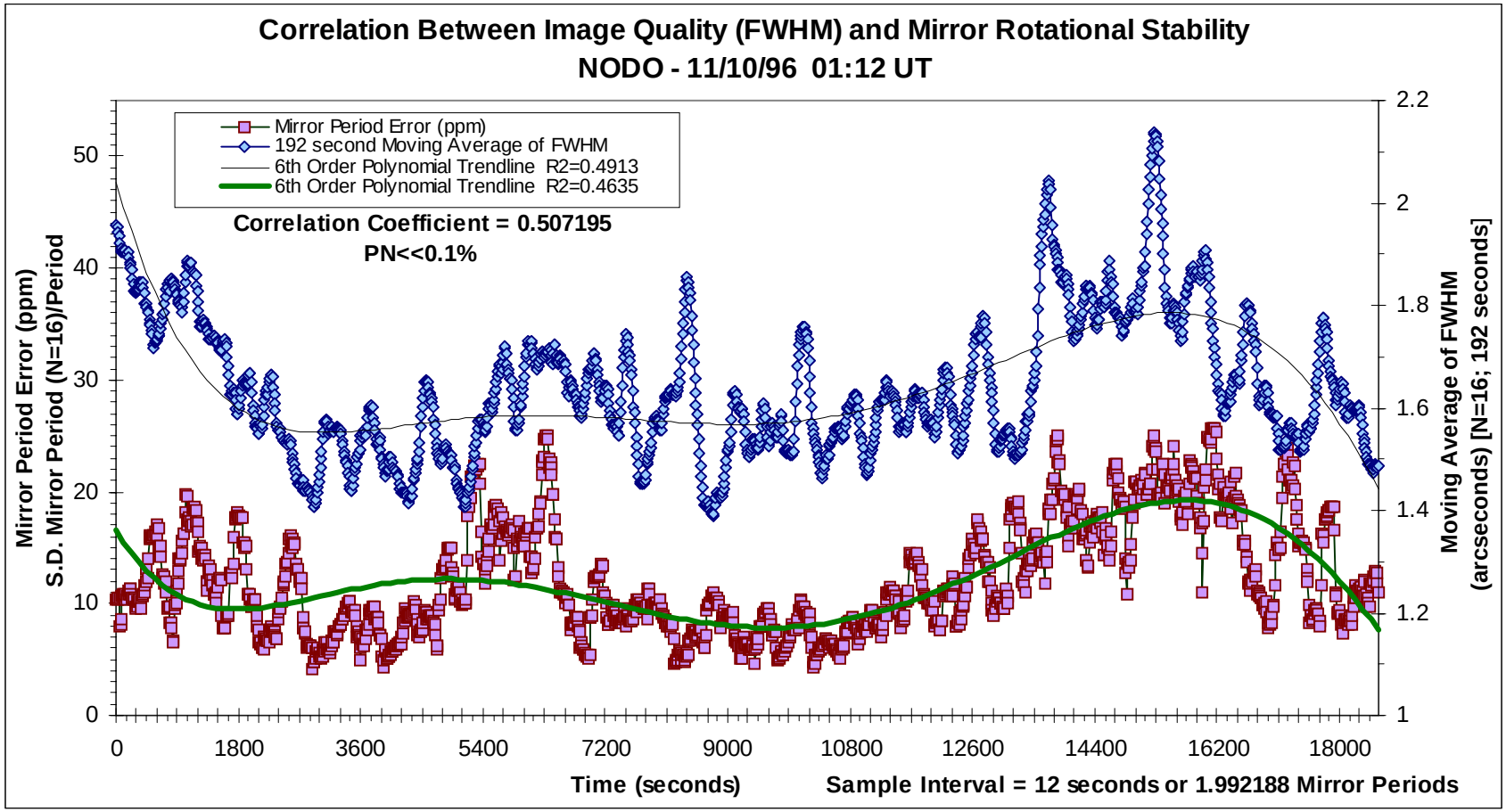

Figure III.D-4. The correlation between instability of the mirror rotational period and image quality. The upper trace (blue) is a 192 second moving average of the FWHM of stellar images taken from a TDI scan acquired while the mirror rotational period was recorded (both at 12 sec intervals). The lower trace (pink) is the standard deviation of each 16 samples (192 secs) of the mirror rotational period normalized by the mean rotational period to yield a relative measure of the mirror rotational instability (ppm). The traces correlate with >99.9% confidence. The correlation is subject to the added influence of atmospheric seeing. Several uncorrelated FWHM peaks are presumably related to poor seeing.

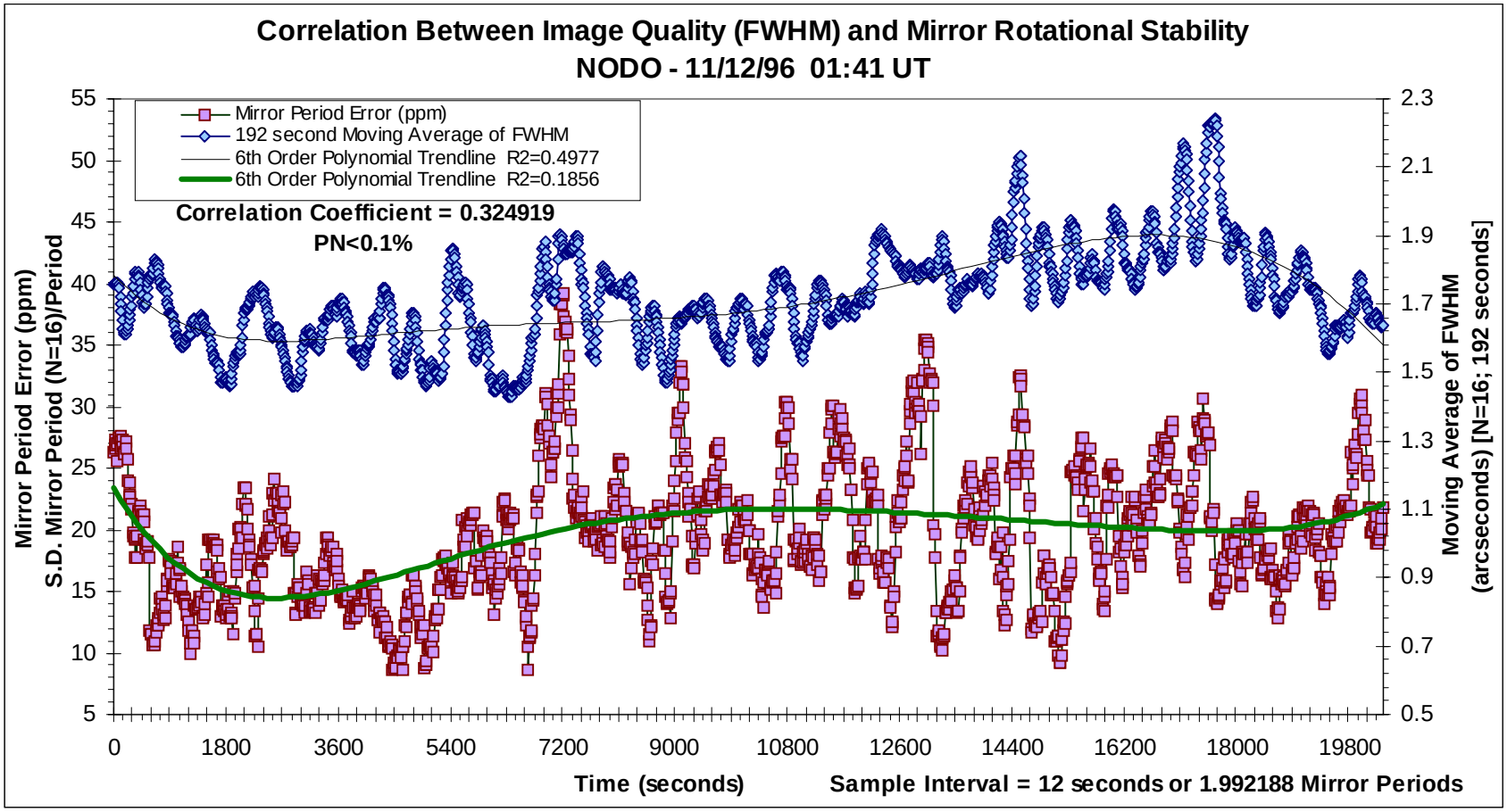

Figure III.D-5. The correlation between instability of the mirror rotational period and image quality. The upper trace (blue) is a 192 second moving average of the FWHM of stellar images taken from a TDI scan acquired while the mirror rotational period was recorded (both at 12 second intervals). The lower trace (pink) is the standard deviation of each 16 samples (192 seconds) of the mirror rotational period normalized by the mean rotational period to yield a relative measure of the mirror rotational instability (ppm). The traces correlate with >99.9% confidence. The correlation is subject to the additional influence of atmospheric seeing.

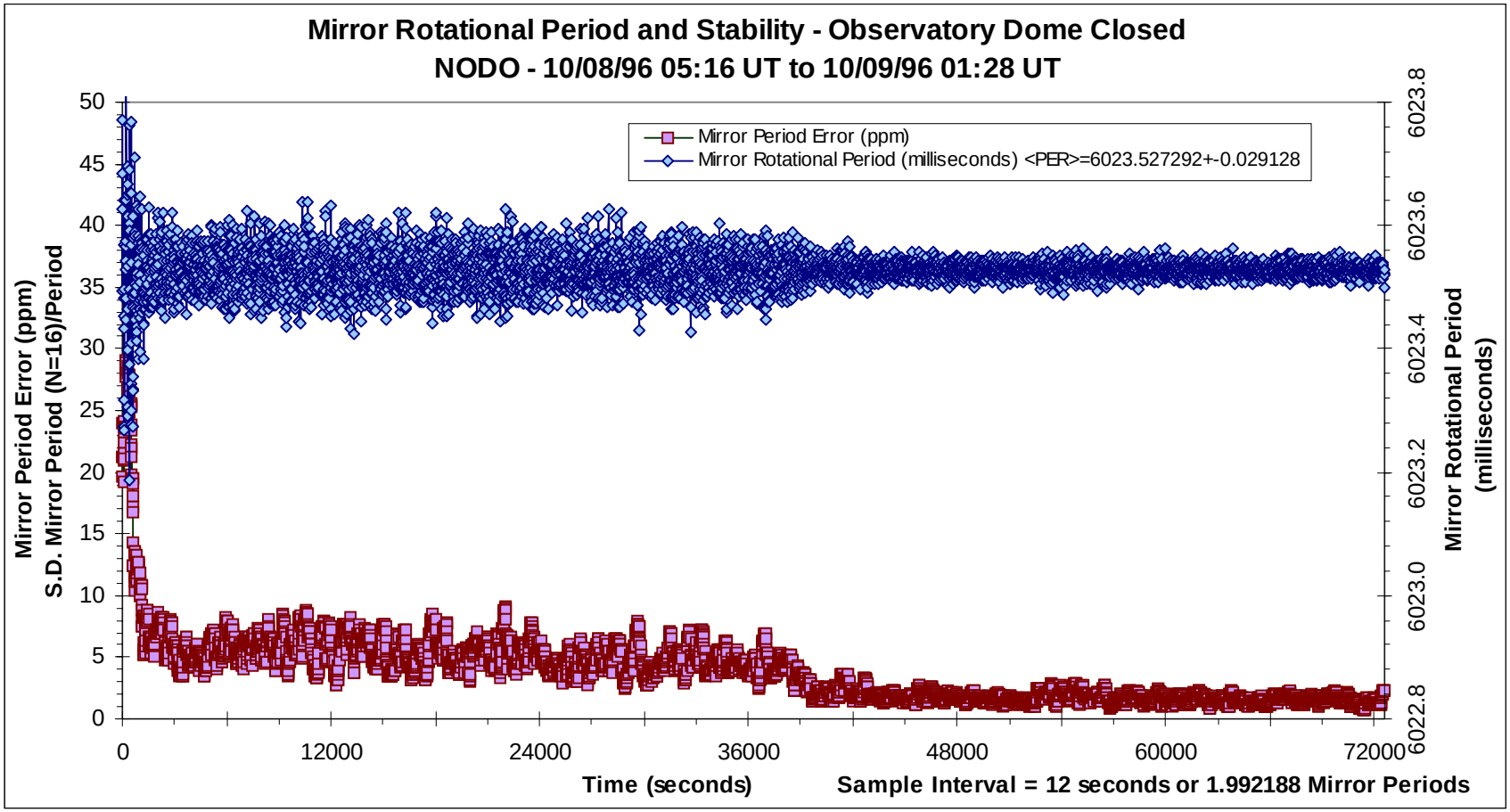

Figure III.D-6. The stability of the mirror rotational period with the dome sealed. The mirror period (upper trace; blue) is recorded at 12 second intervals. The lower trace is the standard deviation of each 16 samples (192 sec) of the mirror period normalized by the mean rotational period to yield a relative measure of the mirror rotational instability (ppm). As the dome is closed, the rotational instability is 10 to 25 ppm, declining to the 5 ppm for ~10 hours, then declining further to 1 to 2 ppm . This non-static behavior is probably related to external winds leaking into the dome cavity, since the quiescent period occurs during the daytime when solar induced diurnal heating would be most extreme.

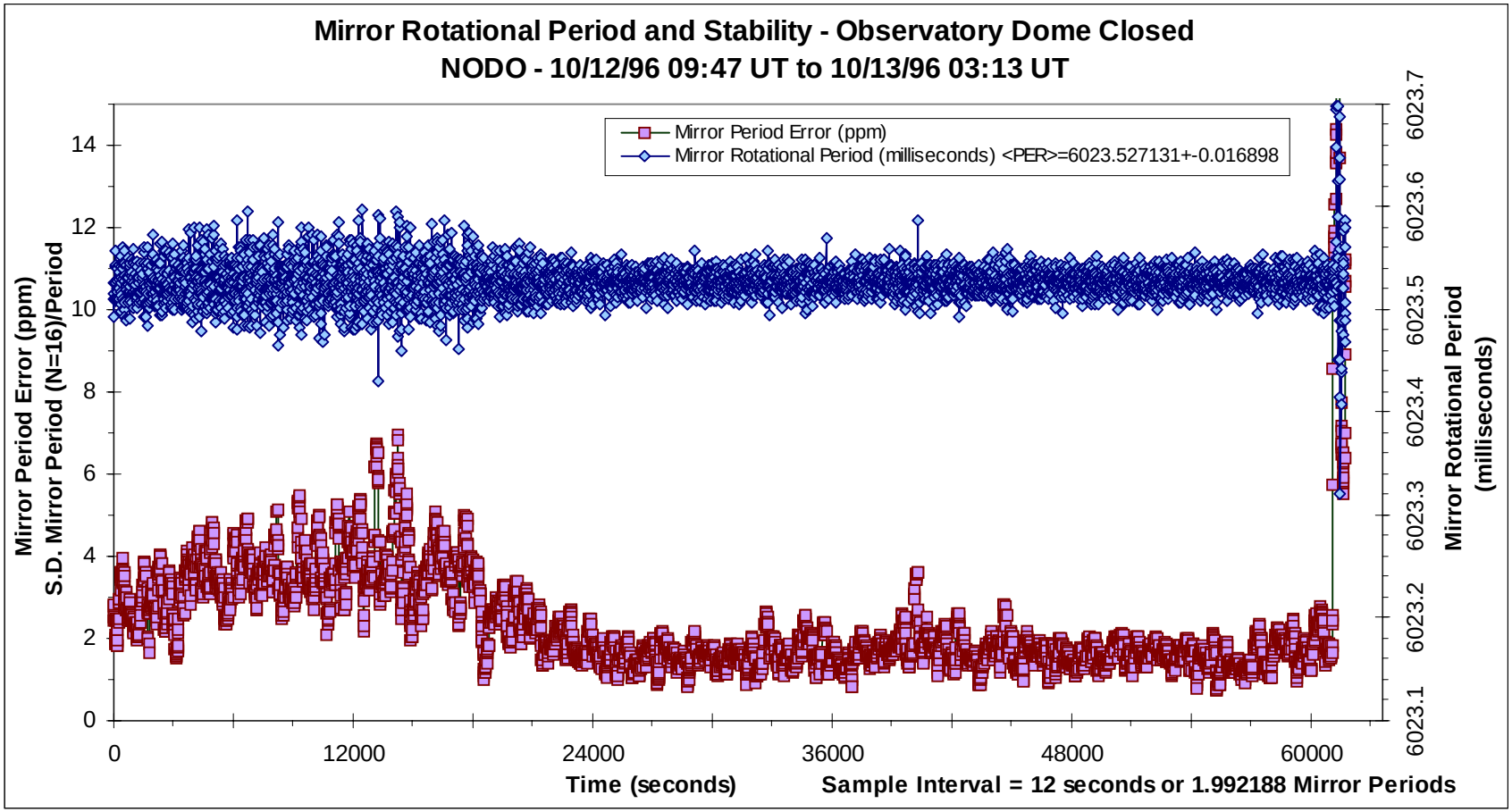

Figure III.D-7. The stability of the mirror rotational period with the dome sealed for several days. The mirror period (upper) is recorded at 12 second intervals. The lower trace is the standard deviation of each 16 samples (192 seconds) of the mirror period normalized by the mean rotational period to yield a relative measure of the mirror rotational instability (ppm). The rotational instability rises from 2.5 to 4 ppm initially, then gradually declines to the 1.5 ppm where it remains until the dome is re-opened, causing a rapid increase in rotational instability. The instability occurs at nighttime and thus is likely due to wind leakage since its does not correlate with solar diurnal heating and cooling.

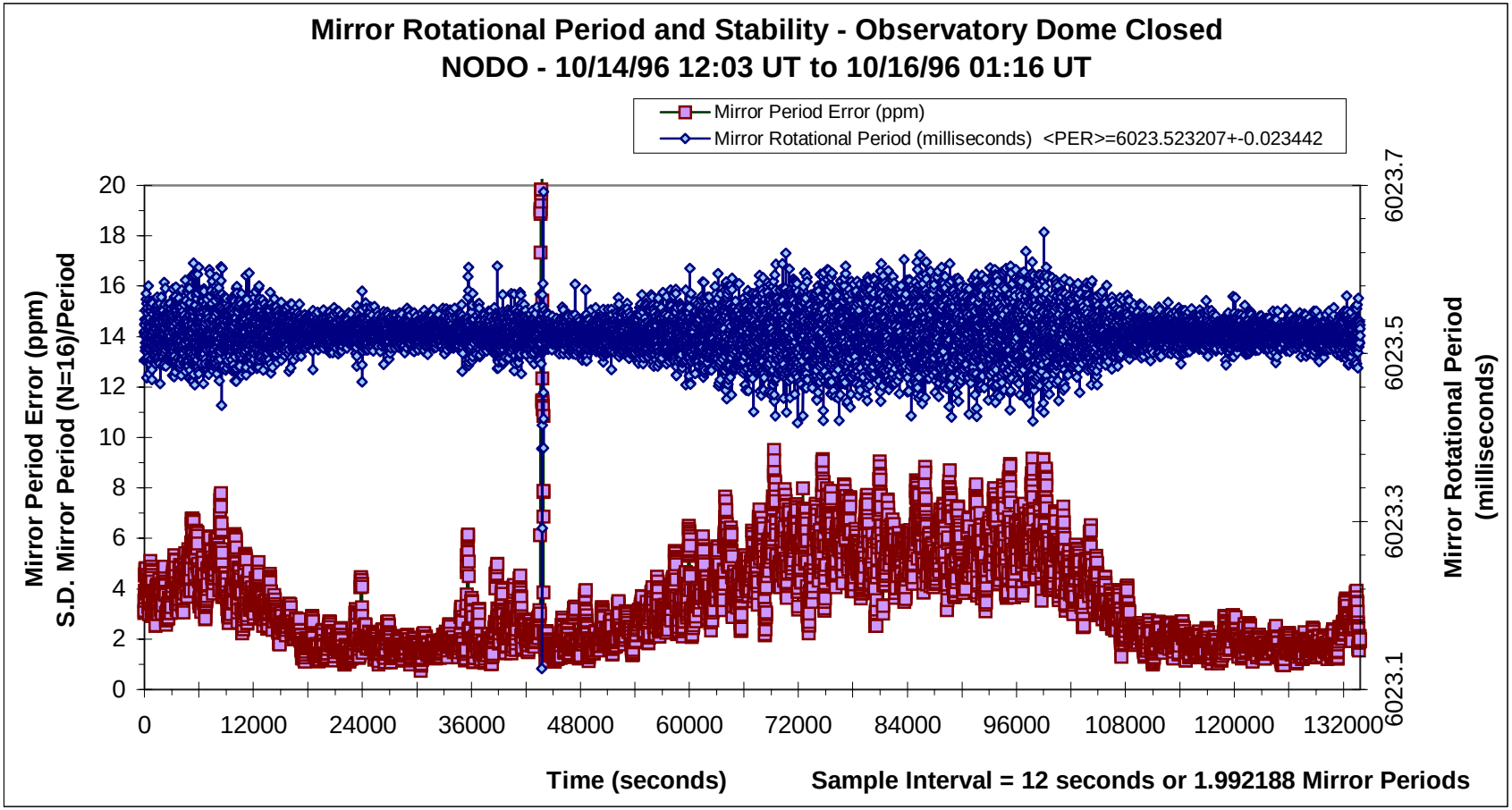

Figure III.D-8. The stability of the mirror rotational period with the dome sealed for several days. The mirror period (upper) is recorded at 12 second intervals. The lower trace is the standard deviation of each 16 samples (192 secs) of the mirror rotational period normalized by the mean rotational period to yield a relative measure of the mirror rotational instability (ppm). The mirror rotational instability varies between 1.5 and 6 ppm with an approximately 24 hour period. This non-static behavior may be related to external winds leaking into the dome cavity, since the period of instability occurs in the evening rather during solar heating. High external nighttime winds seem the most likely cause.

E. Entrance Pupil Aberrations – Mirror Surface Waves and Above Surface Effects

A variety of wave types have been observed on the surface of the NASA Liquid Mirror under point source illuminated Focault and Ronchi testing at the mirror's radius of curvature in the laboratory at NASA-JSC. These surface waves, as well as convective and atmospheric seeing phenomena existing independent of the mirror surface, have also been observed via illumination by off-axis stars during routine astronomical data acquisition at NODO. All of these phenomena have the effect of reducing the optical quality by either altering the parabolic surface in the case of waves, or introducing wave front errors in the case of either convective currents in the dome or atmospheric seeing.

The surface waves consist of primarily spiral and concentric wave formations that are present at all times. The spiral waves possibly arise from vortices that develop in the boundary layer of air immediately above the rotating mirror surface. They are intrinsic to the rotating Hg mirror/air system (or water mirror/air system as seen in Section II.B) and therefore difficult to mitigate. The concentric waves are induced by vibrations of the mirror assembly and pier and have been significantly reduced at the NODO installation by stiffening the substructure. There also exist secondary waves that can arise from any transitory event such as a gust of wind, an impact to the mirror surface by debris, or a change in mirror rotational velocity. With the exception of an occasional insect impact, these secondary waves have been almost completely eliminated at NODO by proper shielding of the mirror and stable rotational velocity control.

Phenomena immediately above the Hg surface consists of convective air currents

emanating from the CCD control electronics package mounted in the prime focus assembly above the center of the mirror. Faint waves of heated air with a lower index of refraction can be seen streaming from the vicinity of the prime focus assembly. A cooling jacket has been proposed to mitigate this problem. The normally engaged mirror brake solenoid located beneath the mirror's northern perimeter is an additional source of convective heating, but it dissipates only 6 watts and the effects have never been seen in the entrance pupil images.

Of greatest significance to any large astronomical mirror are the effects of dome and atmospheric seeing. The former is caused by convective air currents that arise when the mirror, dome, and external environment are not in thermal equilibrium. While the effects of dome seeing have never been observed in the entrance pupil images, exhaust fans are used at NODO to aid the equalization process. It has been observed at major observatories (Hickson PC) that mirror seeing is reduced when the primary mirror is maintained at temperature slightly below ambient (no more than a $2\ ^{0}C$ differential). This results in a descending laminar column of air in the region above the mirror. The installation of a closed-cycle cold fluid circulating system beneath the liquid mirror at NODO is being considered to evaluate this effect.

Unlike dome seeing, the effects of atmospheric seeing are readily seen in the entrance pupil images acquired at NODO. A mottled pattern of light and dark cells or striations of typically 5 to15 cm scale length can be seen in the pupil. Depending upon the night or time of night, the pattern can vary between random fluctuations of light and dark

areas to a unidirectional rapid motion with light and dark streamers elongated in the direction of motion. This mottled appearance arises from wave front errors between atmospheric seeing cells of characteristic dimension R_0 (Fried 1966). The wave front errors induced by atmospheric seeing represents the fundamental limiting factor to the performance of the LMT or any large astronomical mirror. An adaptive optics (AO) system involving a wave front sensor and compensating tip-tilt mirror has been proposed (Hickson PC) to remove the primary seeing component.

1) Dispersion Relation

Before describing the physical properties and possible causes of the waves observed on the liquid mirror, two theoretical dispersion relations are presented so that a comparison can be made with the observations.

For a non-rotating system, Landau and Lifshitz (1959) describe the dispersion relation involving both gravity and capillary waves as:

$$\varpi_{LL}^{\ 2} = (gk + \frac{\alpha k^3}{\rho})\tanh(kh) \qquad \text{(III.E.1a)}$$

Where:

ϖ_{LL} = angular frequency of the wave (radians/sec) (Landau and Lifshitz case)

k = wave number

g = gravitational acceleration (981.67 $cm/\sec^2$ at NODO)

α = surface tension of Hg (485 dyne/cm at 21.5 ^0C)

ρ = density of Hg (13.546 g/cm^3 at 20 ^0C)

h = depth of the Hg layer (cm) (0.225 cm at JSC; 0.161 cm at NODO)

Normally this expression can be simplified for two wavelength regimes where (kh) is large and small relative to unity, but the properties of the waves observed on the NASA liquid mirror (0.148 < (kh) <2.07) as described later in this section do not generally allow this simplification. The group and phase velocity are thus:

$$V_G = \frac{\partial \varpi}{\partial k} = \frac{1}{2\varpi_{LL}}\left[(g + \frac{3\alpha k^2}{\rho})\tanh(kh) + (ghk + \frac{\alpha h k^3}{\rho})\sec h^2(kh)\right] \qquad \text{(III.E.1b)}$$

$$V_P = \frac{\varpi}{k} = \frac{\varpi_{LL}}{k} = \sqrt{(\frac{g}{k} + \frac{\alpha k}{\rho})\tanh(kh)} \qquad \text{(III.E.1c)}$$

Hickson (PC) has derived the dispersion relation for the rotating fluid case:

$$\varpi_H{}^2 = 4\Omega^2 + ghk^2 + \frac{\alpha h k^4}{\rho} \qquad \text{(III.E.1d)}$$

Where:

ϖ_H = angular frequency of the wave (radians/sec) (Hickson case)

Ω = angular velocity of rotating system (radians/sec)

(= 1.043 radians/sec for the NASA-LMT)

The group and phase velocity for the Hickson derivation are thus:

$$V_G = \frac{\partial \varpi}{\partial k} = \frac{1}{2\varpi_H}(2ghk + \frac{4\alpha hk^3}{\rho}) \qquad \text{(III.E.1e)}$$

$$V_P = \frac{\varpi}{k} = \frac{\varpi_H}{k} = \sqrt{\frac{4\Omega^2}{k^2} + gh + \frac{\alpha hk^2}{\rho}} \qquad \text{(III.E.1f)}$$

These theoretical results will be compared with the empirical measurements later in this section.

2) Spiral Waves – Possible Generation Mechanism

Numerous experiments and theoretical analyses have been conducted of fluids contained between concentric rotating cylinders and spheres, or bounded by a rotating disk or disks (Greenspan 1968). By extension, these treatments, coupled with a study performed on a high-speed rotating disk with an impressionable surface, have suggested a possible explanation as to the cause of the spiral waves observed on the surface of the

NASA liquid mirror and other mirrors (Girard and Borra 1997). Figure III.E.2-1 shows an example of these waves as observed from the radius of curvature on the NASA-LMT primary mirror at NASA-JSC. Further examples are shown later in this section.

It has been proposed that the spiral wave pattern observed on a rotating fluid results from a series of horizontal roll vortices in the boundary layer associated with the rotating medium or media. These vortices represent an instability in the boundary layer either interior to the fluid or at a fluid-fluid interface. Generation of the instability requires there be flow relative to the global motion of the system. The spiral pattern has been induced in several ways. Faller and Kaylor (1966) did so by rotating a sealed water tank which possessed an inner and outer annulus acting as a sink and source respectively. By varying the source strength and thereby generating a relative flow within the rotating fluid, separate from the global rotation of the system, Faller and Kaylor were able to artificially create an instability in the fluid boundary layer. This instability manifested itself as a series of spiral waves within the rotating fluid. This example is interesting as it lends insight as to the mechanism by which the spiral pattern may be generated in the LMT system. Since the water tank was sealed, the pattern could not originate in the water-air boundary, but instead was artificially induced in the boundary layer interior to the fluid itself via the source-sink flow. In the case of the LMT, where there is no source or sink flow of Hg, the instability may arise from the relative flow between the Hg surface and the inferior rotation of the air above it. Figure III.E.2-2 shows the spiral patterns, called Class B waves, observed by Faller and Kaylor.

Gregory, Stuart, and Walker (1955) observed the spiral pattern on a rapidly

NASA-LMT @ JSC: Focault Test -Spiral Waves Near Mirror Perimeter

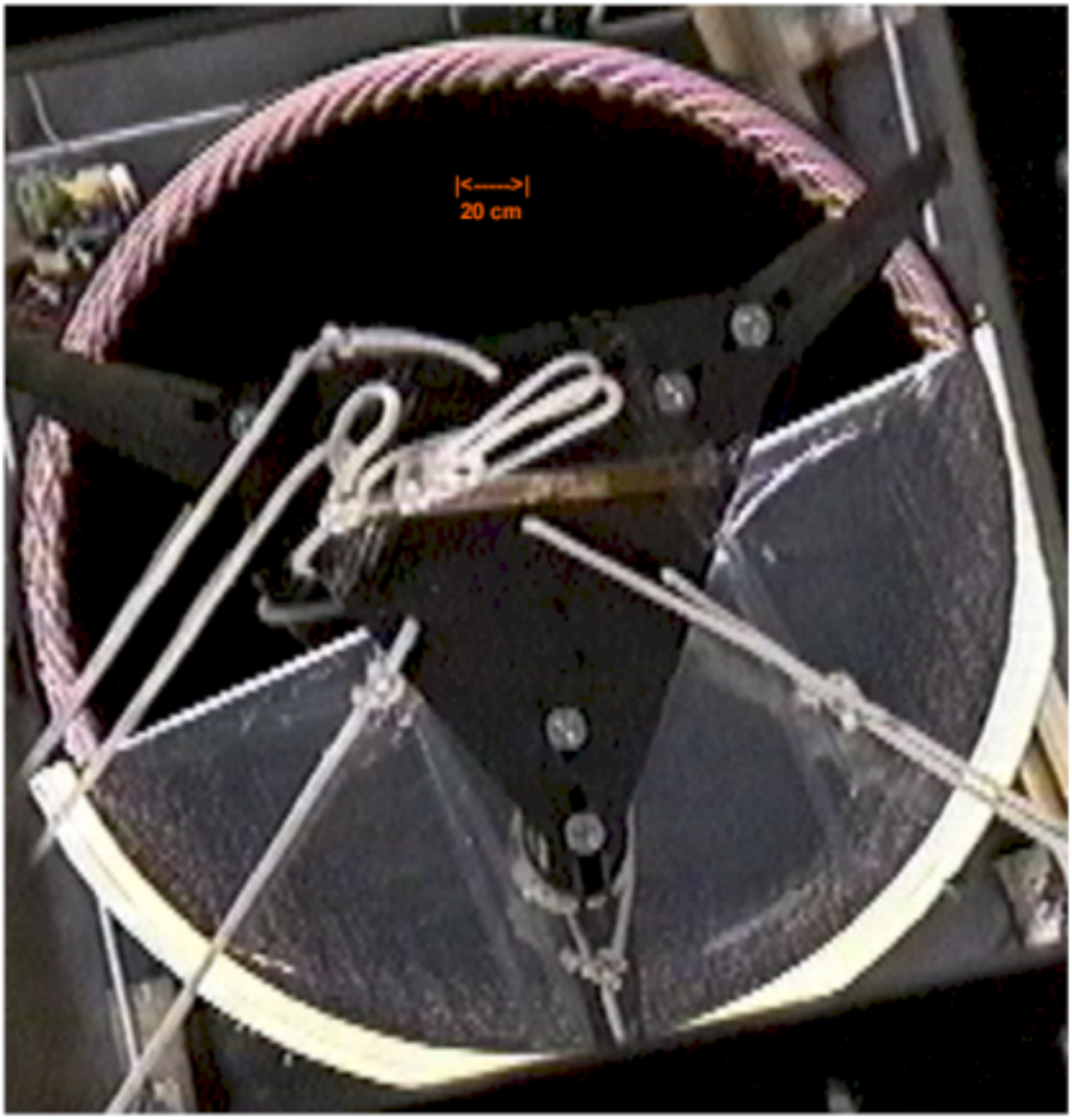

Figure III.E.2-1. Edge zone (92% radius) of the liquid mirror under point source illumination at the radius of curvature. The spiral waves are clearly visible with $\lambda \cong 4.5$ to 6.8 cm at this range of radial position (138 to 150 cm). The waves intersect the mirror rim at an angle of $\theta = 26.5$ degrees and the entire pattern rotates at an azimuthal velocity slightly inferior to the mirror rotational velocity. At the mirror perimeter, the transverse wave phase speed is approximately 34 cm/sec directed toward the mirror interior. The spiral waves are possibly due to vortices created by non-laminar airflow over the Hg fluid surface. Concentric vibration-induced waves ($\lambda \cong 1.7$ cm) emanating from the mirror rim are also visible in the upper left quadrant. A mylar cover obscures the lower half of the mirror. Rotation: CCW

Class B Spiral Waves in a Sealed Water Tank

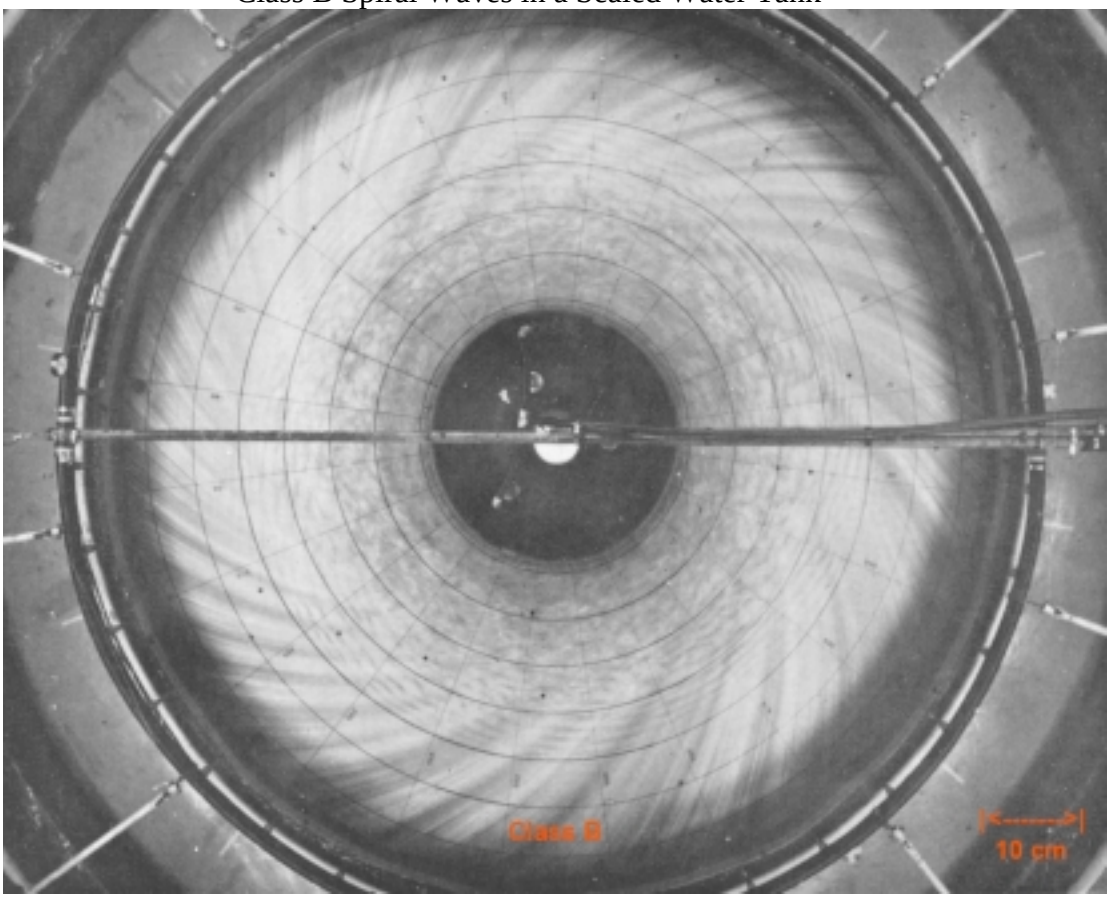

Figure III.E.2-2. Faller and Kaylor (1966) demonstrated the formation of horizontal roll vorticies in the boundary layer of water in a rotating sealed water tank 7.6 cm deep and 91 cm in diameter. The instability giving rise to the spiral formation (Class B waves) was generated by introducing an azimuthal source and sink flow originating and terminating at the perimeter and inner annulus respectively. The critical Reynolds number at which the spirals form agrees well with the comparable formation of spiral waves on the NASA-LMT resulting from azimuthal air flow over the rotating mirror. Rotation: CCW

rotating disk covered with an impressionable china clay material. In this example, the mechanism is thought to be purely rotational vortices in the air above the disk. The spiral pattern observed in the LMT may similarly result from vortices in the air alone impinging on the Hg surface or the Hg may also possess vorticity (the latter is discounted below). The spiral pattern as observed by Gregory and the theoretical cross-section of the vorticies which may reside in the boundary layer above the spinning disk are shown in Figure III.E.2-3.

The water tank experiments as well as similar experiments performed by Tatro and Mollo-Christensen (1967) using only air as a medium yielded a set of criteria for the onset of the instability. Following their analysis and that of Greenspan, we must first characterize the boundary layer thickness. This was first done by Ekman (Greenspan 1968) who found:

$$\delta = L \cdot \sqrt{E} = \sqrt{\frac{\nu}{\Omega}} \qquad \text{(III.E.2a)}$$

Where:

δ = Boundary layer thickness

E = Ekman number

ν = kinematic viscosity (dynamic viscosity/density)

($0.0012\ cm^2/\text{sec}$ for Hg and $0.150\ cm^2/\text{sec}$ for air at $20\ ^0C$)

Ω = angular velocity of the system (1.043 radians/sec for the NASA-LMT)

Spiral Waves on a High-speed Rotating Disk

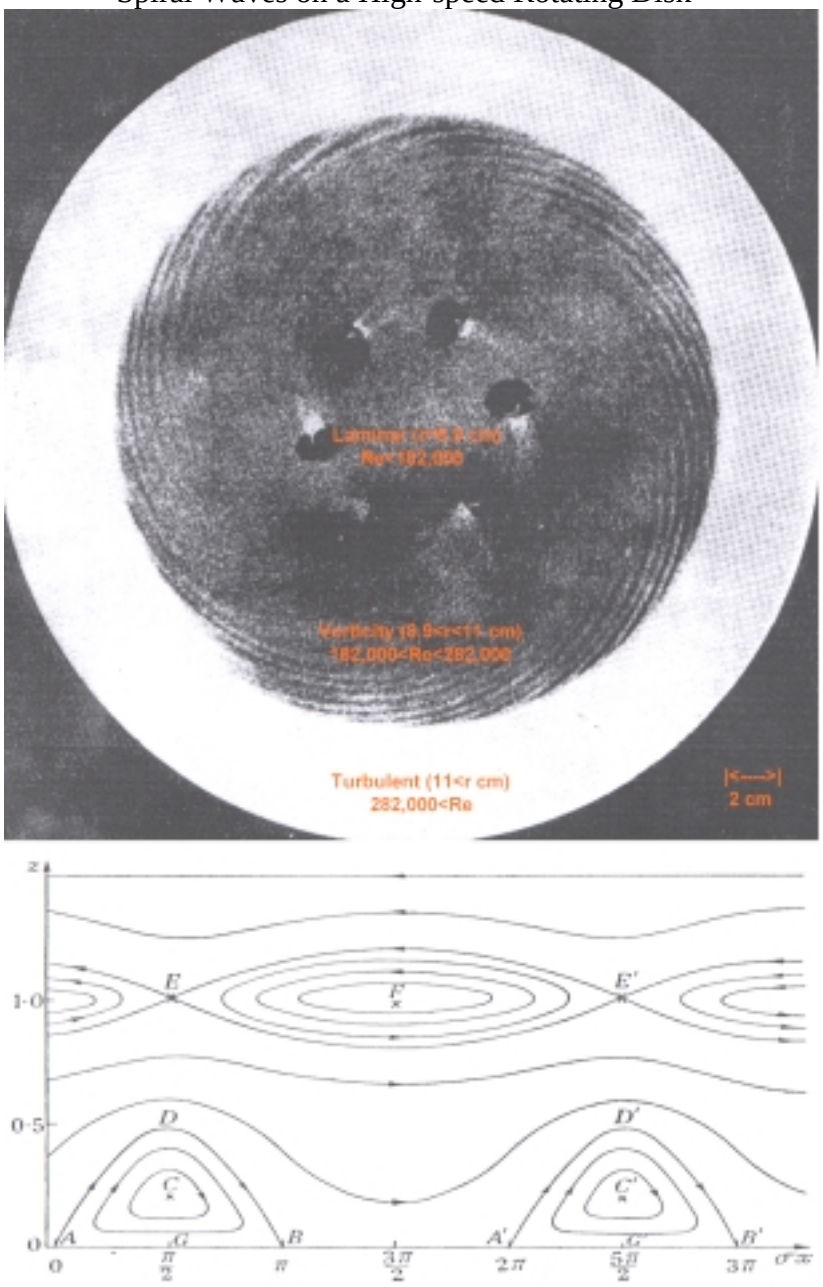

Figure III.E.2-3. Gregory et al. (1955) demonstrated the formation of horizontal roll vorticies in the boundary layer of air above a rotating disk. In this example, the 30 cm diameter disk with an impressionable surface was rotating at 335 radians/sec. Three distinct zones of flow are visible: Laminar (0<r<8.9 cm), Vorticity (8.9<r<11 cm), and Turbulent (11<r cm). The Reynolds number (Re) for the onset of vorticity is higher than for the LMT spirals, but this may be due to increased coupling between the air-Hg interface versus the air-china clay interface in this experiment. The lower figure shows the cross-section of the air boundary layer vorticity as derived analytically by Gregory et al. The disk surface is at z=0. This cannot be an exact analog to the LMT spirals because these spirals are logarithmic and the LMT spirals are linear. Rotation: CCW

L = characteristic length of the system

The Ekman number is a gross measure of the relative importance of the viscous and Coriolis forces within the rotating system. It is also the inverse Reynolds number (R_E) for the global rotation:

$$R_E = \frac{\Omega L^2}{\nu} \qquad \text{(III.E.2b)}$$

Furthermore we can define a Rossby (ε) number characterizing the ratio of the convective acceleration to the Coriolis force. This gives an estimate of the importance of non-linear terms:

$$\varepsilon = \frac{U}{\Omega L} \qquad \text{(III.E.2c)}$$

Where:

U = the relative velocity of a particular motion (U = 0 for solid body rotation)

For the case of the water and air tanks, the Rossby and Reynolds numbers were defined to characterize the relative azimuthal flow (V_ϕ) induced in the boundary layer by the source and sink flows. Thus:

$$\varepsilon = \frac{V_\phi}{\Omega L} \qquad \text{and} \qquad R_E = \frac{\delta \cdot V_\phi}{\nu} \tag{III.E.2d}$$

Using a hot wire anemometer to measure δ and V_ϕ, it was determined empirically from the Faller and Kaylor source and sink water tank experiments that the boundary layer became unstable when the Reynolds number exceeded a critical value given by:

$$R_{E_{CRIT}} = 124.5 + 3.66 \cdot \varepsilon \tag{III.E.2e}$$

To see if the LMT satisfies this criteria, first consider the Hg fluid alone. At 20 ^0C the kinematic viscosity of Hg is 0.0012 cm^2/sec. The characteristic scale of the LMT system is taken as the mirror radius of 150 cm and the angular velocity (Ω) is 1.043 rad/sec. Substituting into III.E.2a yields an Ekman boundary layer thickness (δ) of 0.339 mm. Now there are two plausible sources for Hg motion relative to the global angular velocity of the LMT system. The motion could arise from infinitesimal angular velocity instabilities caused by wind and convective air currents as discussed in the previous section (III.D). The relative motion could also arise from drag induced on the Hg at the Hg-air interface. Experiments performed at NASA-JSC and NODO wherein a marker was placed on the Hg surface, indicated no discernable relative motion of the Hg surface with respect to the mirror container even after several weeks of observation. Thus the Hg

is essentially in solid body rotation implying V_ϕ is either zero or exceedingly small and therefore the Hg alone cannot satisfy the critical Reynolds number criteria. Thus it seems plausible that the Hg boundary layer is stable and there is no vorticity within the Hg fluid itself.

When considering the air at the Hg-air interface, a different result is obtained. At 20^0C the kinematic viscosity of air is 0.150 $cm^2/\sec$. The characteristic scale and angular velocity of the Hg-air interface is essentially the same as for the Hg alone, thus from equation III.E.2a the air boundary layer thickness (δ) is 3.79 mm. Assuming the airabove the mirror is essentially stationary prior to the onset of instability, the relative velocity of the air to the Hg surface is purely azimuthal and is related to the radial position (r) by simply:

$$V_\phi = r\Omega \qquad \text{(III.E.2f)}$$

Substituting into equation III.E.2d yields the following expression for the Reynolds number and Rossby number for the Hg-air interface:

$$R_E = \frac{\delta \cdot r \cdot \Omega}{\nu} = 2.64 \cdot r \qquad \text{and} \qquad \varepsilon = \frac{r}{L} \qquad \text{(III.E.2g)}$$

Comparing this expression with equation III.E.2e, we find that the onset of instability ($R_E > R_{E_{CRIT}}$) occurs when r > 47.6 cm corresponding to an azimuthal linear velocity (V_ϕ)

of 49.64 cm/sec.

This is a very interesting result, since the spiral wave pattern observed on the NASA liquid mirror appears to exist permanently for radii greater than 64.5 cm(V_ϕ = 67.3 cm/sec) and only intermittently at radii interior to this value. Presumably the intermittent aspect may be due to brief wind gusts which temporarily cause V_ϕ to increase such that $R_{E_{CRIT}}$ is exceeded for small radii. A very similar pattern is observed on other liquid mirrors as in the case of Borra's laboratory 1.5 m f/2 mirror as shown in Figure III.E.2-4.

The extraordinary agreement between the LMT results and the empirical observations made of the water and air tanks, is further supported by the observations of Gregory regarding spiral wave impressions made by air on rotating disks. Using the alternate Reynolds number definition given in equation III.E.2b, Gregory found that the spiral pattern existed for Reynolds numbers in the range:$1.78x10^5 \le R_E \le 2.99x10^5$. Below this range the air flow was laminar, above this range the flow was turbulent. Defined in this way, these values exceed the range of Reynolds numbers for the air above the NASA-LMT which maximize at $1.56x10^5$ for the perimeter. The marginal disagreement may arise from the difference in interaction between the air-china clay interface in Gregory's experiment and the air-Hg interface in the liquid mirror case. It is conceivable that there may be stronger coupling between the air and Hg causing the boundary layer instability and roll vorticies to occur at lower Reynolds numbers. It will be interesting to observe the spiral wave pattern on the 6m LZT. The maximum Reynolds number for air at the mirror perimeter will be $4.43x10^5$ which could possibly place the air

Spiral Waves on a 1.5 m f/2.0 Liquid Mirror

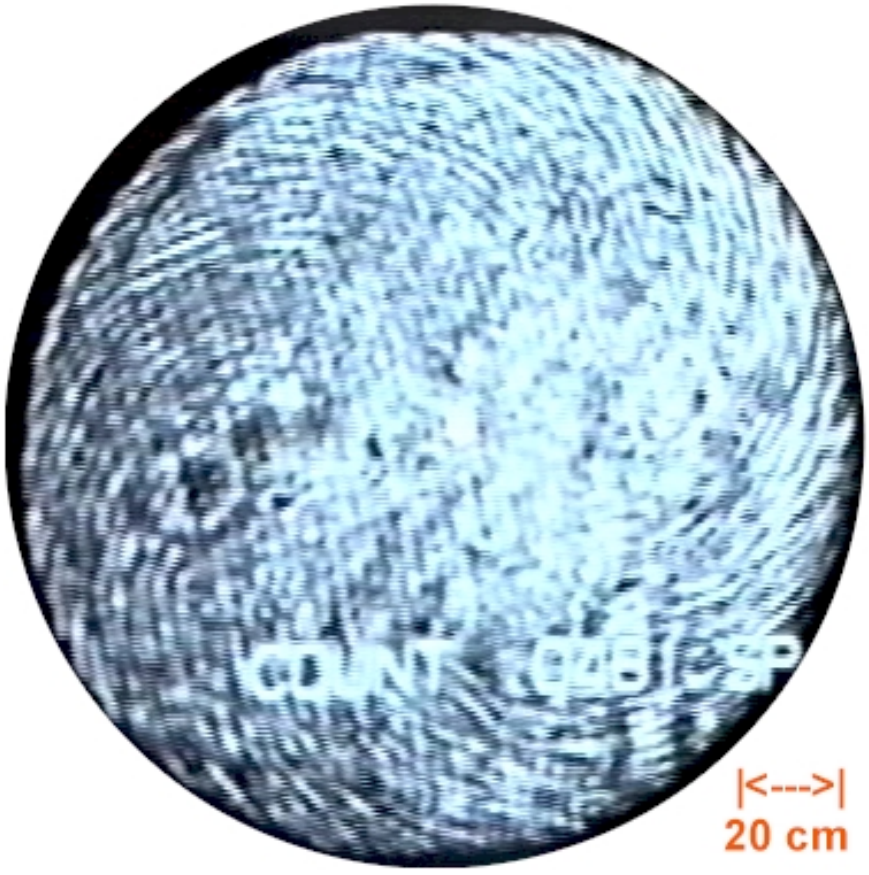

Figure III.E.2-4. Spiral waves observed on a 1.5 m f/2.0 liquid mirror in Borra's laboratory. The mirror is rotating with angular velocity Ω =1.28 radians/sec. The form of these spirals appears identical to that of the NASA-LMT in the sense of a linear relationship between radial position and azimuthal angle. The spiral pattern appears to terminate at a radial position of approximately 37.5 cm corresponding to a linear velocity of 48 cm/sec. This is close to what is observed on the NASA liquid mirror where the stable spiral pattern exists for r>64.5 cm corresponding to a minimum linear velocity of 67.3 cm/sec. Rotation: CW

flow in the turbulent domain. This may or may not have a more adverse effect on the mirror surface than the rotational vorticies.

An additional piece of supporting evidence for the roll vorticity explanation of the spiral waves observed on liquid mirrors comes from Landau and Lifshitz (1959). They derive an expression for the stability of a tangential discontinuity between two fluids of different densities (ρ_1, ρ_2) and surface tensions (α_1, α_2), moving relative to each other. In order for the flow to be laminar, in the case where α_2 is negligible, the following expression regarding the relative velocities (U) must hold:

$$U \leq \sqrt[\frac{1}{4}]{\frac{4\alpha g(\rho_1 - \rho_2)(\rho_1 + \rho_2)^2}{\rho_1^2 \rho_2^2}} \qquad \text{(III.E.2h)}$$

Substituting the known values for air and Hg into this equation, we obtain: $U \leq 72.4 cm/\sec$. This is remarkably close to the approximately U $\leq$ 67.3 cm/sec air-Hg velocity differential at which spiral waves only occur intermittently on the NASA-LMT. For air-Hg differentials above this value, where presumably the air flow is no longer laminar, the spiral waves are a permanent feature on the mirror.

3) Spiral Waves – Empirical Measurements

Independent of the underlying cause of the spiral wave pattern, a quantitative description has been made of their properties. This assessment was made by measuring numerous images acquired both at the radius of curvature of the LMT when located at

NASA-JSC and at a position laterally displaced from the focal position at NODO. The Focault images were most useful in determining wavelengths and velocities, whereas the Ronchigrams enabled an approximate determination of the wave amplitudes.

Radius of Curvature and Off-Axis Focault Results:

The spiral wave parameters along with a comparison of the dispersion relation predictions of Hickson and Landau and Lifshitz are listed in Table III.E.3-1. Figures III.E.3-1 through 6 show some of the images from which the parameters were derived. It is evident from the table that the spiral waves (within the indicated accuracy of the measurements) appear to have a constant frequency (Column C) independent of the measured wavelength (Column B). This implies that the group velocity is zero and the measured velocity is purely phase velocity. Therefore the spiral pattern consists of stationary waves. Furthermore, the wavelength and frequency dependence does not follow either the Landau and Lifshitz or the Hickson dispersion relations. These two factors lend further support in favor of the argument that the spiral pattern is induced by vorticity in the air above the mirror and is not caused by gravity or capillary waves propagating on the rotating mirror surface. The same is not true of the concentric waves as discussed in the next section. It is interesting to note from the figures in column G that the azimuthal velocity of the spiral wave pattern is less than the azimuthal velocity of the liquid mirror at the same measured locations. Thus the spiral wave pattern rotates at an angular velocity slightly inferior to the mirror rotational velocity. The magnitude of the inferior rotation

Table III.E.3-1. Parameters for Spiral Waves Observed on the NASA-LMT

A	B	C	D	E	F	G	H	Landau and Lifshitz			Hickson		
Radial Position r (cm)	$\lambda \pm 0.17cm$ $[k(cm^{-1})]$	$\nu \pm 10\%$ (Hz) $[\varpi]$ (rad/s)	$V_G \pm 10\%$ $cm/\sec$	$V_P \pm 10\%$ $cm/\sec$	α (deg)	$1-\frac{V_\phi}{r\Omega}$	$-V_R$ $\frac{cm}{\sec}$	$[\varpi_{LL}]$ (rad/s)	V_G $\frac{cm}{\sec}$	V_P $\frac{cm}{\sec}$	$[\varpi_H]$ (rad/s)	V_G $\frac{cm}{\sec}$	V_P $\frac{cm}{\sec}$
150	6.8 [0.92]	5 [31.4]	~ 0	34	26.5	0.903	30.4	[13.8]	15.2	15.0	[14.0]	15.4	15.3
143	4.75 [1.32]	5 [31.4]	~ 0	23.75	27.7	0.926	21.0	[19.9]	15.6	15.1	[20.3]	16.2	15.4
130	3.4 [1.85]	5 [31.4]	~ 0	17.0	30.0	0.937	14.7	[28.4]	16.2	15.3	[28.5]	17.9	15.8
115	2.0 [3.14]	5 [31.4]	~ 0	10	33.1	0.954	8.38	[50.5]	18.2	16.1	[54.4]	21.9	17.3
95	1.36 [4.62]	5 [31.4]	~ 0	6.8	38.3	0.957	5.34	[79.2]	20.6	17.1	[91.6]	28.5	19.8

Table III.E.3-1. The measured parameters for the spiral waves observed on the NASA-LMT and a comparison with the dispersion relation predictions of both Landau and Lifshitz and Hickson. The parameters are based on images of the liquid mirror acquired at the radius of curvature under point source illumination at NASA-JSC .The Hg layer thickness was 2.25 mm (now 1.61 mm). The apparent frequency of the waves is independent of wavelength indicating stationary behavior.

NASA-LMT @ JSC: Spiral Wave Motion at r = 115 cm

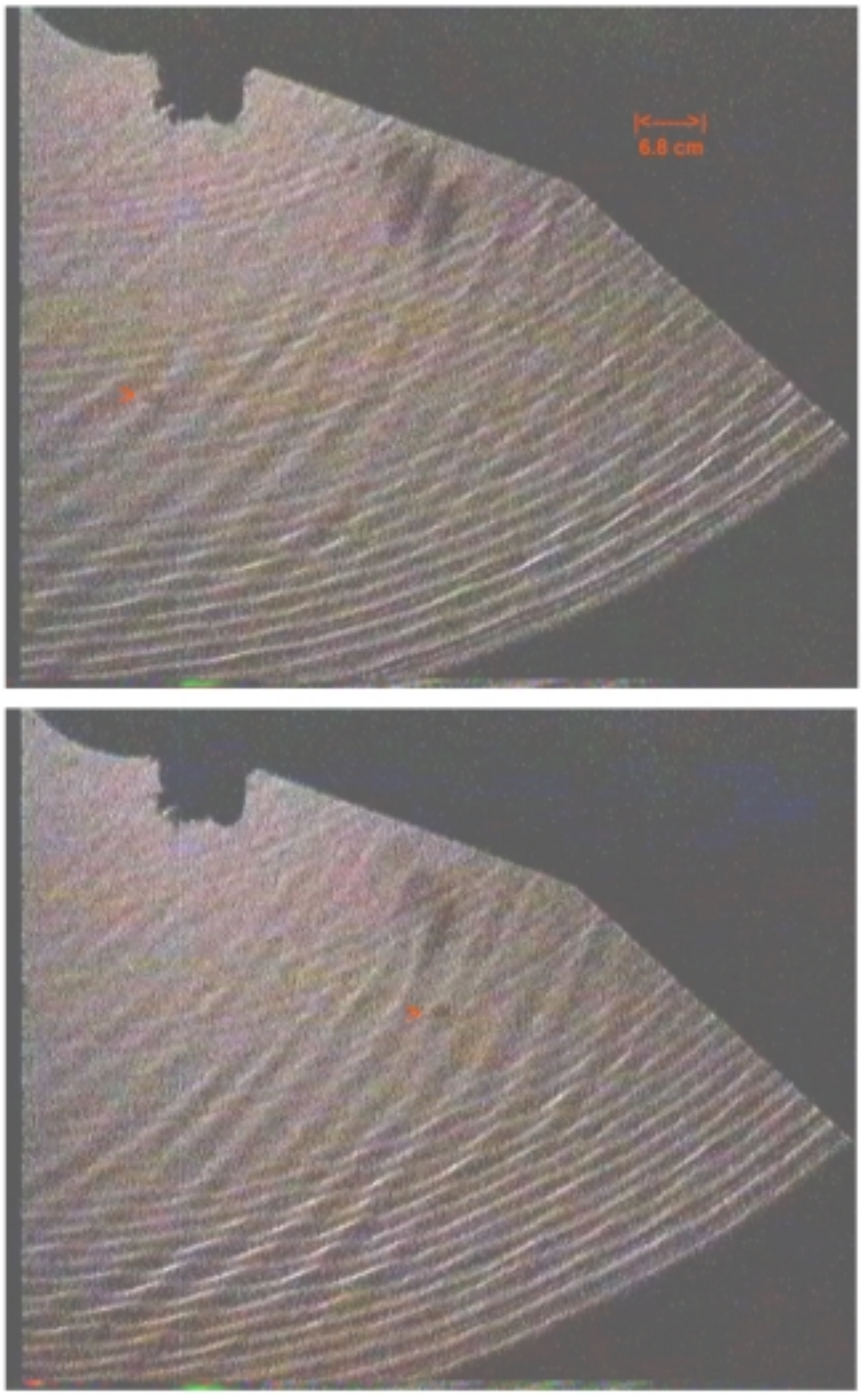

Figure III.E.3-1. Two video frames of the NASA liquid mirror acquired under point-source illumination at the radius of curvature. The red arrows indicate a reference point on the mirror surface (r=115 cm) against which the spiral wave motion was measured. The frames are separated by 0.2 seconds (6 video frames) in which time the spiral wave-front moved 1 wavelength (2 cm) implying a frequency of 5 Hz. Rotation: CCW

NASA-LMT @ JSC: Spiral Wave Motion at r = 143 cm

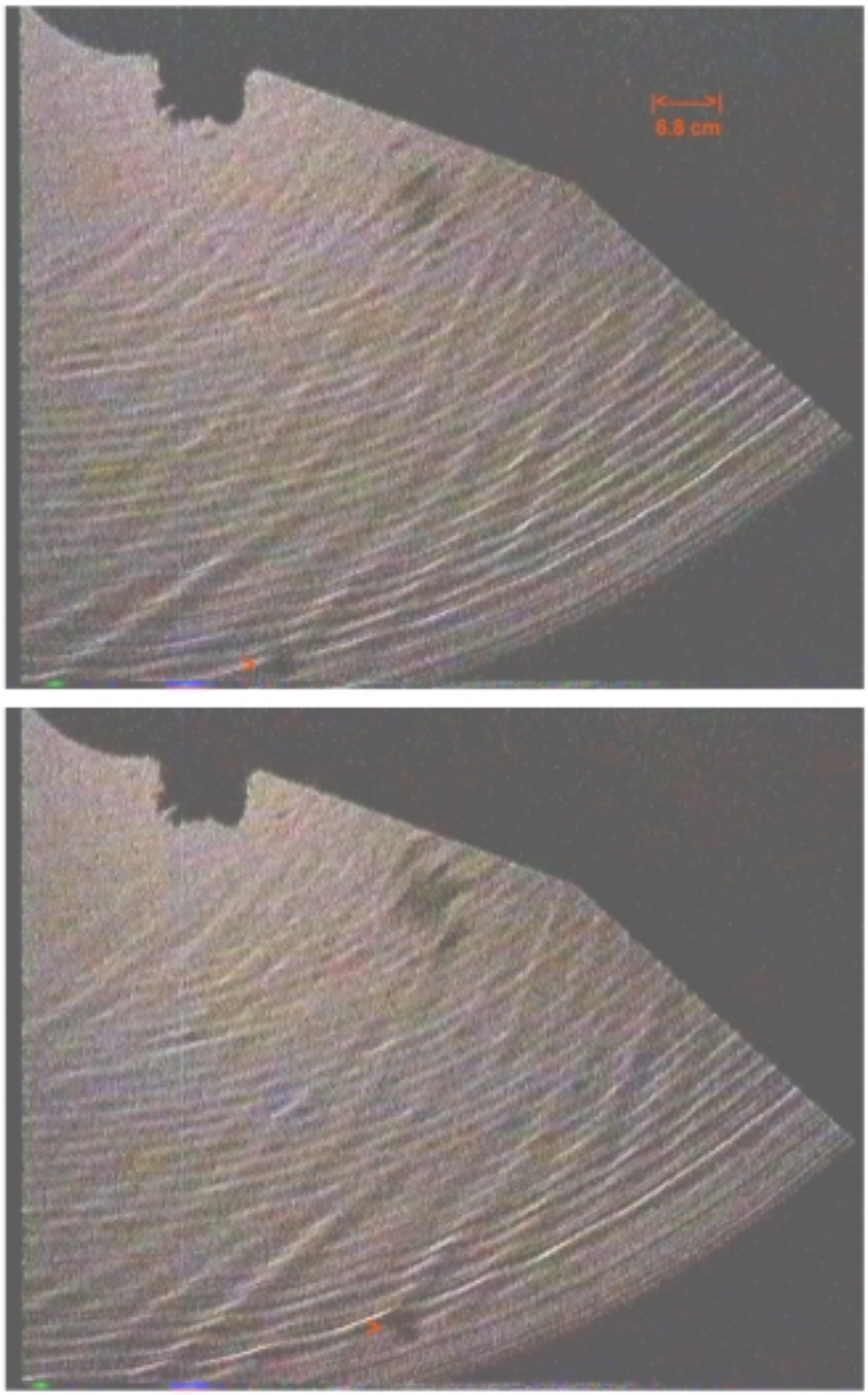

Figure III.E.3-2. Two video frames of the NASA liquid mirror acquired under point-source illumination at the radius of curvature. The red arrows indicate a reference point on the mirror surface (r=143 cm) against which the spiral wave motion was measured. The frames are separated by 0.067 seconds (2 video frames) in which time the spiral wave front moved 1/3 wavelength (4.75/3 cm) implying a frequency of 5 Hz. (Continued in the next figure.)

NASA-LMT @ JSC: Spiral Wave Motion at r = 143 cm

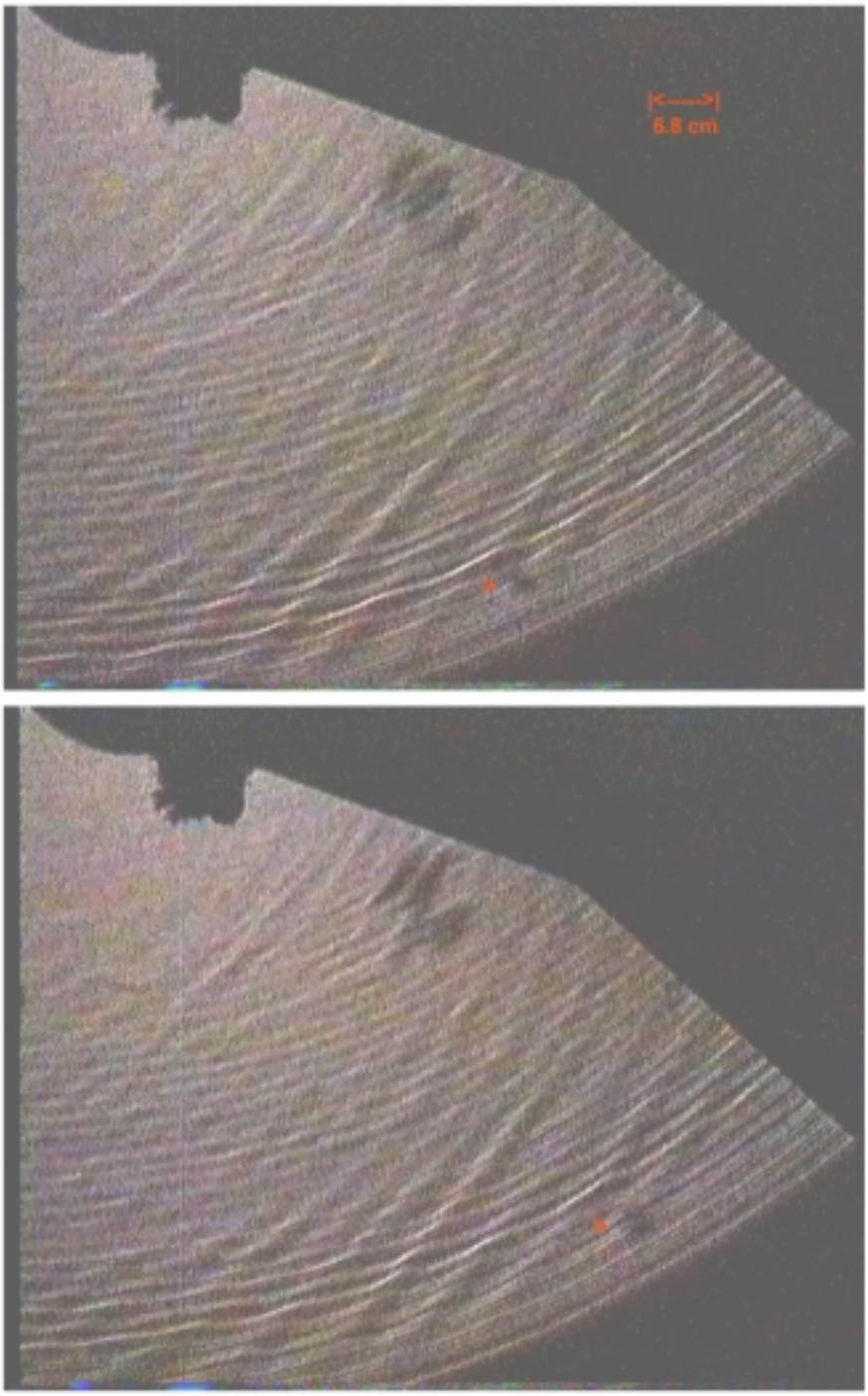

Figure III.E.3-3. Continuation from the previous figure. The red arrows indicate a reference point on the mirror surface (r=143 cm) against which the spiral wave motion was measured. The frames are separated from the previous suite and from each other by 0.067 seconds (2 video frames). The spiral wave front moved 1 wavelength (4.75 cm) over the complete 4 frame (0.2 second) sequence implying a frequency of 5 Hz. Rotation: CCW

NASA-LMT @ NODO: Spiral and Concentric Waves Near Mirror Perimeter

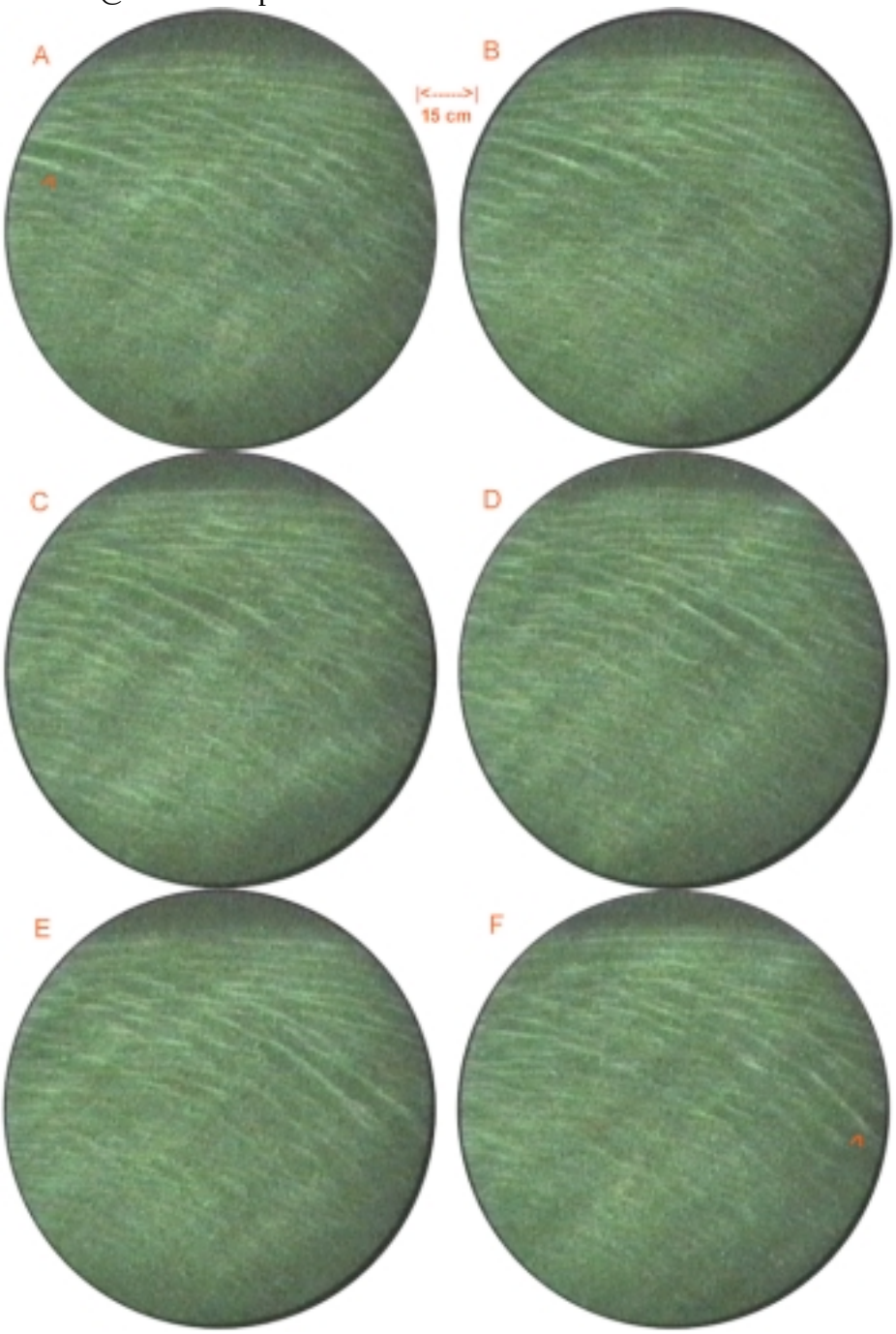

Figure III.E.3-4. Time series of images acquired approximately 3 degrees off-axis with an image-intensified video camera laterally displaced from the focal position at NODO. The sequence demonstrates the inward radial motion ($-V_R$) of a spiral wave front ($\lambda \cong 6$ cm) indicated by the red arrow. These waves are possibly induced by airflow over the rotating mirror surface. Concentric vibration-induced waves emanating from the mirror perimeter are also visible. (Frames separated by 0.1 sec; Rot: CW)

NASA-LMT @ NODO: Spiral and Concentric Waves Near Mirror Perimeter

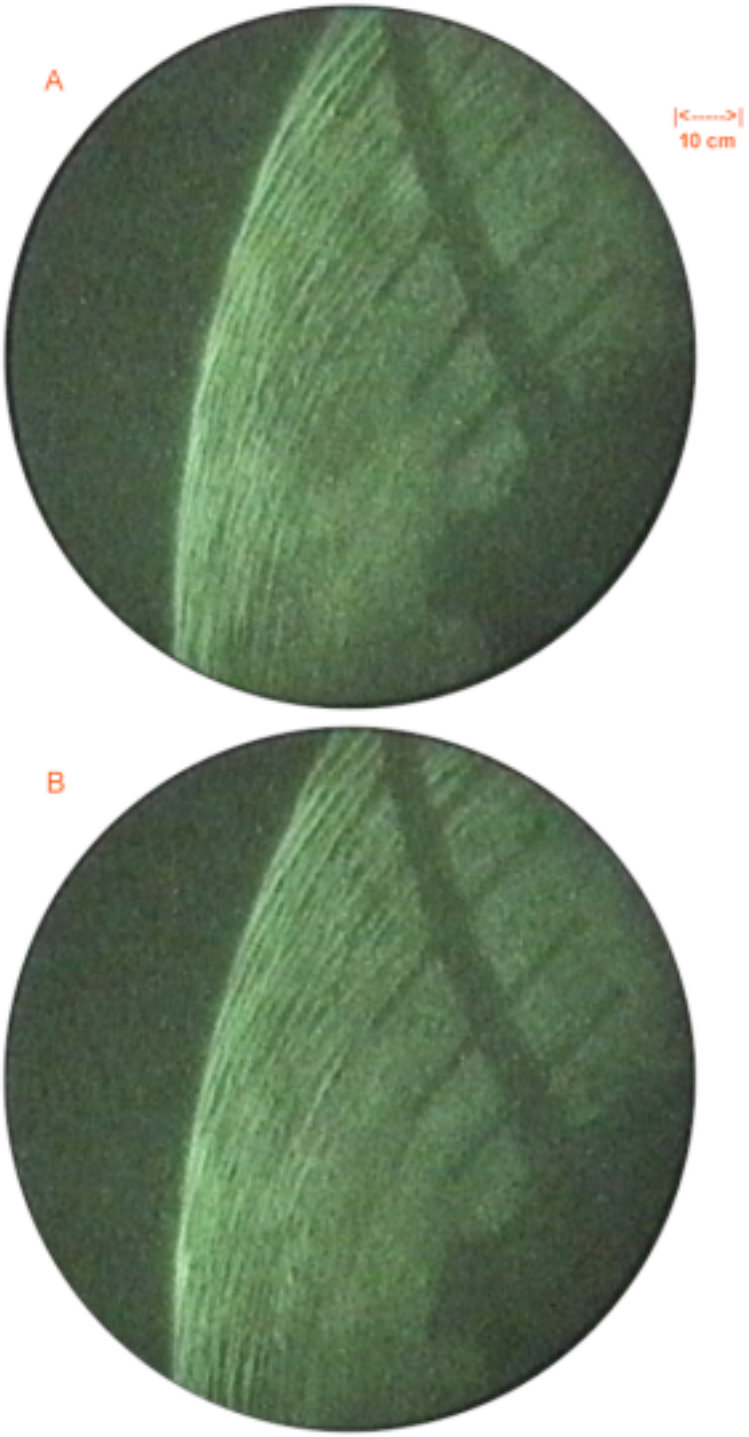

Figure III.E.3-5. Time series of images acquired off-axis at NODO demonstrating a spiral wave front ($\lambda \cong 6$ cm). These waves are possibly induced by airflow over the rotating mirror surface. (Frames separated by 0.1 seconds; Rotation: CW)

NASA-LMT @ NODO: Spiral and Concentric Waves Near Mirror Perimeter

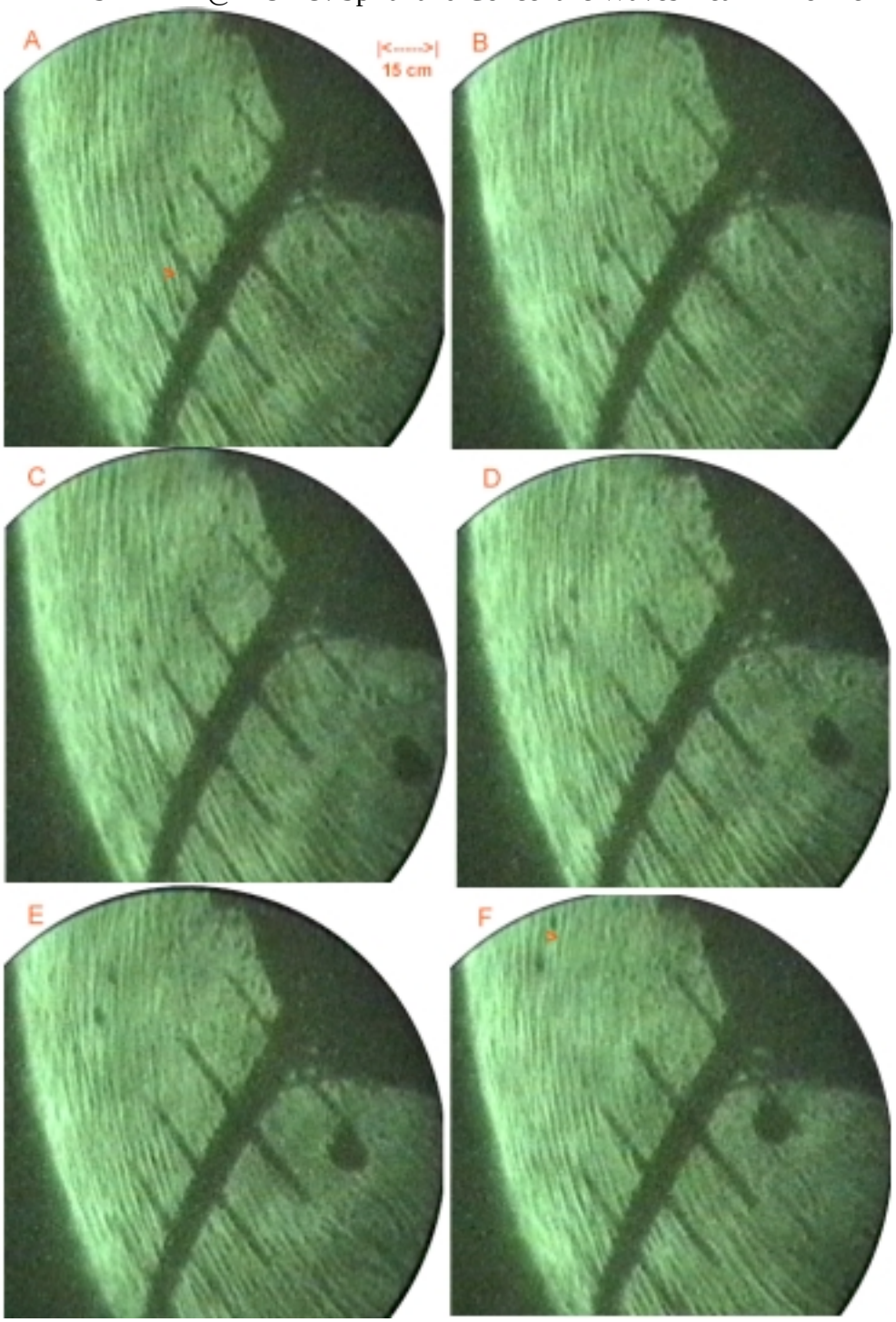

Figure III.E.3-6. Time series of off-axis images demonstrating the inward radial motion of spiral surface waves ($\lambda \cong 2$cm). The motion of the portion of a single wave front is indicated (red arrow). The wave moves inward relative to a small hole (dark) in the Hg surface layer. (Frames separated by 0.1 seconds; Rotation: CW)

maximizes at the mirror perimeter and minimizes at the mirror's central hub where the wave front is purely azimuthal and the intermittent spiral pattern is thereby essentially co-rotating. Borra has observed similar spiral patterns rotating slower than his laboratory liquid mirrors.

Figure III.E.3-7 shows the form and extent of both the permanent and transitory (r < 64.5 cm) spirals. The spiral wave front radial position (r) depends linearly on azimuthal angle (ϕ) and thus the angle between the azimuth vector and the wave front (tangentialangle) is not constant. This is similar to the wave tank results, but is in contrast to the logarithmic spirals observed by Gregory et al (1955). The radial extent of the spirals observed on the rotating disk may not be sufficient to differentiate between logarithmic and linear spirals, hence a possible explanation for the disparity. As also indicated on the graph, the LMT spirals are governed by the following relations:

$$r = 150(1 - \frac{\phi}{2}) \qquad \text{and} \qquad \tan\alpha = \frac{-dr}{rd\phi} = \frac{75}{r} \qquad \text{(III.E.3a)}$$

Where:

r = the radial position of the spiral wave front (cm)

ϕ = azimuthal angle (radians)

α = the angle between the azimuth vector and the wave front

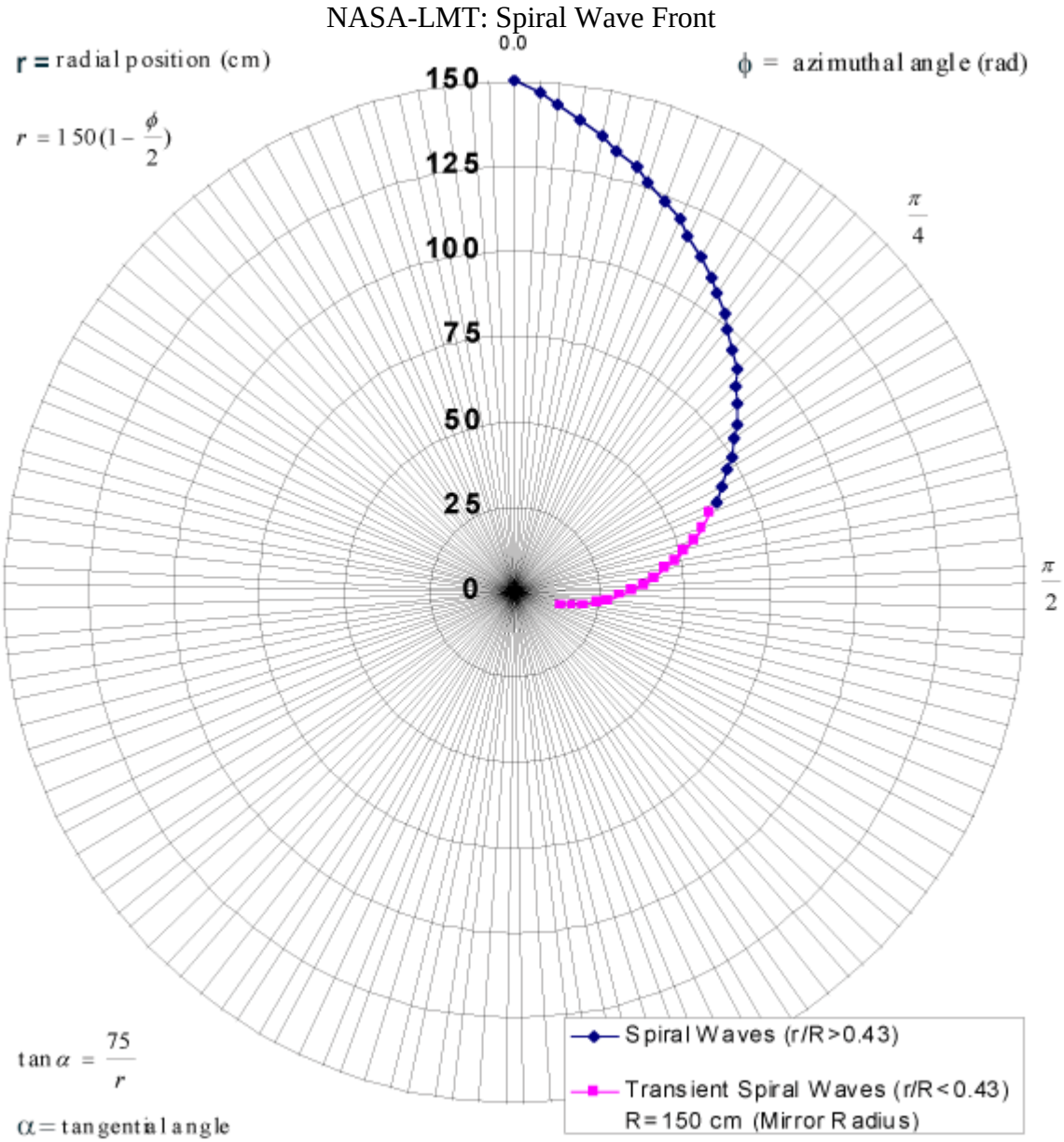

Figure III.E.3-7. The linear form of the spiral waves observed on the Hg surface of the NASA-LMT. The tangential angle (the angle between the wave front and the azimuth vector) varies from 26.5 degrees at the mirror perimeter to 90 degrees at the mirror's center. Waves (pink) extending to the mirror center (r < 64.5 cm) are seen only very occasionally and are presumed due to stray currents of air impacting the mirror and temporarily exceeding the critical Reynolds number for the onset of vorticity. (Rotation: CW)

Ronchigram Results:

By a simple geometric argument, it was possible to obtain an estimate of the spiral wave amplitude at several positions near the mirror perimeter. The estimates are based on a series of images acquired at the NASA-LMT radius of curvature (RC) with a Ronchi grating (20 lines/cm) in place. If the assumption is made that an individual spiral waveform is approximately triangular in shape and that the wave amplitude (A) is small relative to the wavelength(λ), (A<< λ), then the linear peak-to-valley displacement in thegrating lines (LD_{P-V}) caused by a passing wave is related to the amplitude and wavelength of the wave by the expression:

$$WaveAmplitude = A = \frac{LD_{P-V}}{RC} \cdot \frac{\lambda}{4} \qquad \text{(III.E.3b)}$$

This simply states that a tilted planar wave front will displace the observed grating lines by an amount related to its amplitude and wavelength.

The calculated values based upon the Ronchigrams shown in Figure III.E.3-8 are tabulated in Table III.E.3-2. The indicated positions (colored arrows) are shown in the table. The average of the measured amplitude values, independent of radial position, is 241 nm. This is 0.48 waves of green light (0.48 λ @ λ = 0.5 um). Thus these spiral waves have an amplitude comparable to those the aberrations induced by the Coriolis and tilt effects discussed in the first part of this Chapter.

NASA-LMT @ JSC: Ronchigrams of the 3.0 m mirror

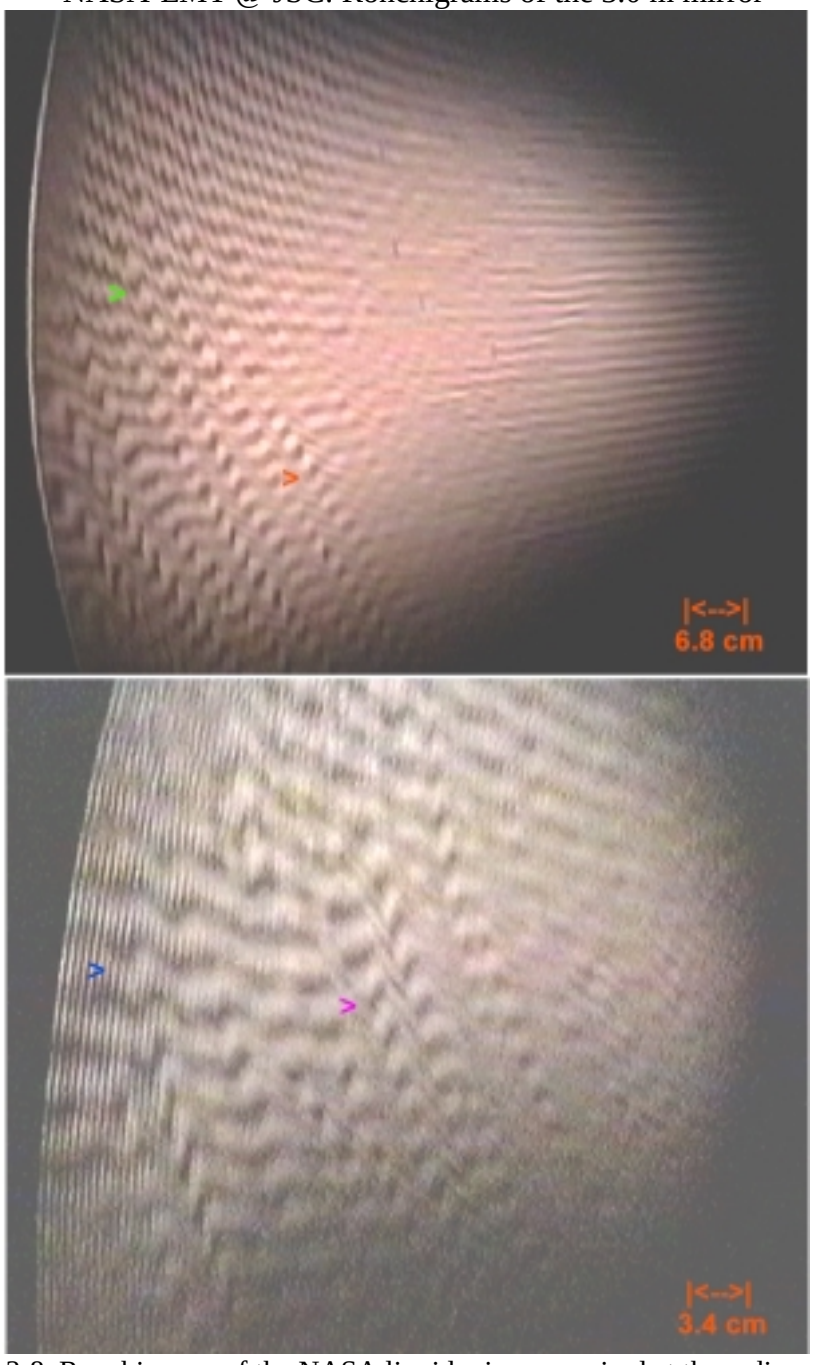

Figure III.E.3-8. Ronchigrams of the NASA liquid mirror acquired at the radius of curvature under point-source illumination with a 20 line/cm Ronchi grating. The arrows indicate reference points at which the spiral wave amplitudes were measured using the simple geometric relation described in the text. As an example, at the pink arrow (r = 133 cm) the spiral wave has displaced the grating lines by 1/2 their separation of 0.05 cm. At the 900 cm radius of curvature, the wave front (if triangular) must be tilted by 0.000007 radians to cause this displacement. By simple geometry, the measured wavelength of 3.5 cm implies a wave amplitude of 243 nm. (Rot: CCW)

Table III.E.3-2

	Radial Position (cm)			
	(Blue)	(Green)	(Pink)	(Red)
	145	136.5	133	118
A (nm)	330	250	243	142

4) Concentric Waves – Empirical Measurements

Table III.E.4-1 lists the concentric wave parameters along with a comparison of the dispersion relation predictions of Hickson and Landau and Lifshitz. Figures III.E.4-1 through 4 show some of the images from which the parameters were derived.

Two types of concentric waves have been observed on the surface of the NASA liquid mirror. They are differentiated by wavelength and oscillating frequency. The short wavelength (SW; $\lambda \cong 0.68$ cm) concentric waves were observed at NASA-JSC but not at NODO. They existed at larger mirror radii ($116 < r < 150$ cm) and emanated from the mirror perimeter traveling radially inward at approximately 30.5 cm/sec with a frequency of approximately 45 Hz. From close inspection of the video data acquired at the radius of curvature under point-source illumination of the mirror, these short wavelength waves appear to dissipate before reaching the inner regions of the mirror ($r < 116$ cm). Since the short wavelength waves do not appear in the off-axis images acquired at NODO, it is assumed that they were caused by environmental forcing specific to the NASA-JSC

Table III.E.4-1. Parameters for Concentric Waves Observed on the NASA-LMT

A	B	C	D	E	F	G	Landau and Lifshitz			Hickson		
Radial Pos r (cm)	$\lambda \pm 0.17cm$ [$k(cm^{-1})$]	$\nu \pm 20\%$ [ϖ]	$V_G \pm 20\%$ $cm/\sec$	$V_P \pm 20\%$ $cm/\sec$	V_ϕ cm/s	$-V_R$ cm/s	[ϖ_{LL}] (rad/s)	V_G cm/s	V_P cm/s	[ϖ_H] (rad/s)	V_G cm/s	V_P cm/s
116-150 (SW; JSC)	0.68 [9.2]	45 Hz [283]	ID (0)	30.5	0	30.5	[189]	27.3	20.6	[276]	52.8	30.0
148.5 (LW)	2.0 [3.14]	15 [94.2]	‘’	30.0	0	30.0	[50.5]	18.2	16.1	[54.4]	21.9	17.3
136 (LW)	1.7 [3.70]	15 [94.2]	‘’	25.5	0	25.5	[60.9]	19.1	16.5	[67.3]	24.3	18.2
119 (LW)	1.53 [4.11]	15 [94.2]	‘’	23.0	0	23.0	[68.9]	19.8	16.8	[77.7]	26.1	18.9
95 (LW)	1.36 [4.62]	15 [94.2]	‘’	20.4	0	20.4	[79.2]	20.6	17.1	[91.6]	28.5	19.8
75 (LW)	1.2 [5.24]	15 [94.2]	‘’	18.0	0	18.0	[92.3]	21.6	17.6	[110]	31.6	21.0
4-29 (LW) (NODO)	1.15 [5.46]	15 [94.2]	‘’	17.3	0	17.3	[88.9]	21.7	16.3	[99.2]	27.6	18.2
0-4 (LW) (NODO)	1.7 [3.70]	15 [94.2]	‘’	25.5	0	25.5	[53.9]	18.0	14.6	[57.0]	20.5	15.4

Table III.E.4-1. Measured parameters for concentric waves observed on the NASA-LMT and a comparison with the dispersion relations of both Landau and Lifshitz and Hickson. The higher radial position (r>75 cm) parameters are based on images of the liquid mirror at JSC with a 2.25 mm Hg layer. The smaller radial position (r<29 cm) values are based on NODO measurements with a 1.61 mm Hg layer. The frequency of the waves appear to be independent of wavelength (stationary behavior), but accuracy is insufficient to make a determination (indeterminant = ID).

NASA-LMT @ JSC: Short Wavelength Concentric Motion at r = 150 cm

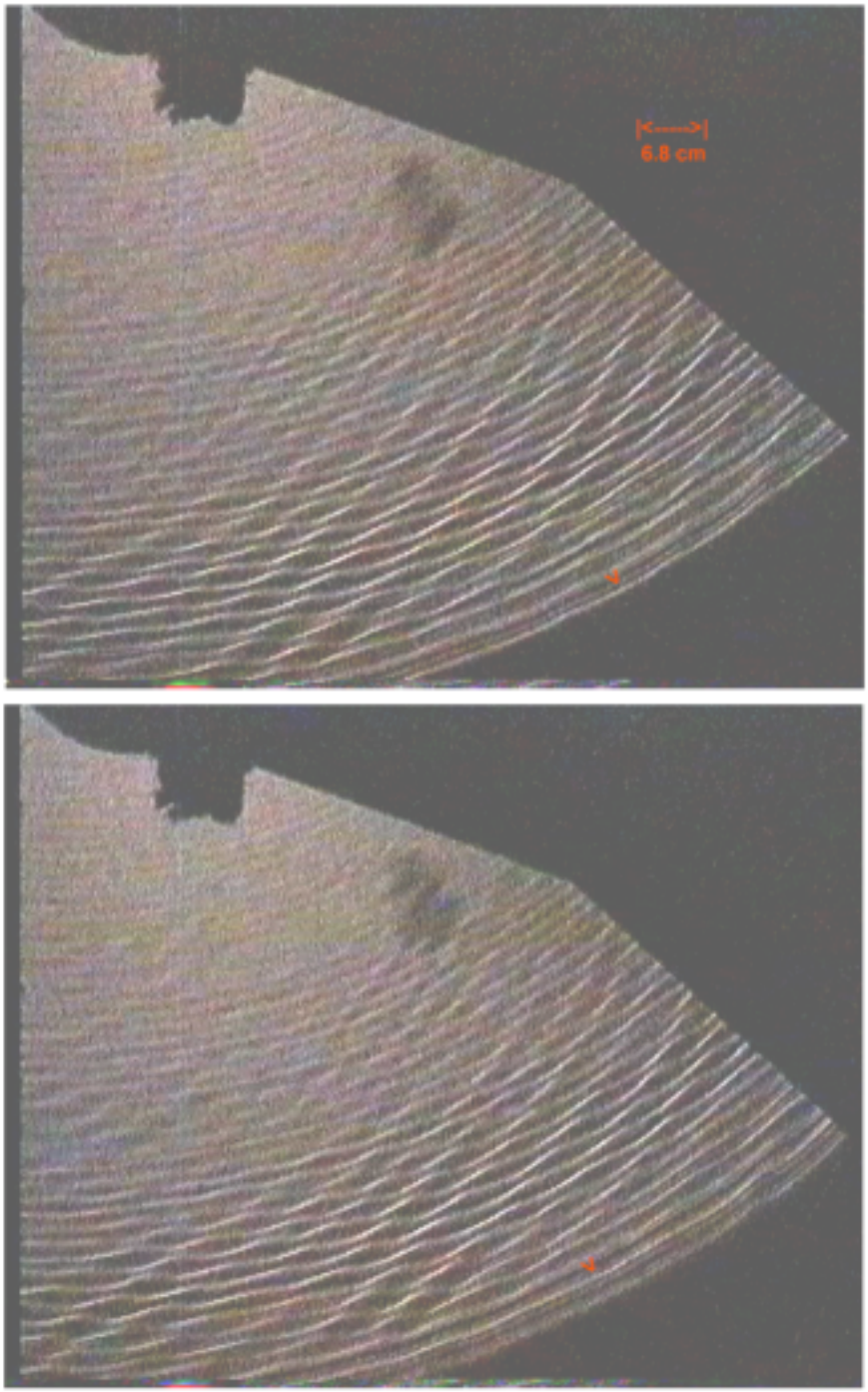

Figure III.E.4-1. Two video frames of the NASA liquid mirror acquired under point-source illumination at the radius of curvature. The red arrows indicate two positions (r=150 and 147.5 cm) on a short wavelength concentric wave against which the wave motion was measured. The frames are separated by 0.067 seconds (2 video frames) in which time the concentric wave front moved radially inward 2.04 cm (3 wavelengths) implying a frequency of 45 Hz. (Rot: CCW)

NASA-LMT @ JSC: Long Wavelength Concentric Motion at r = 148.5 cm

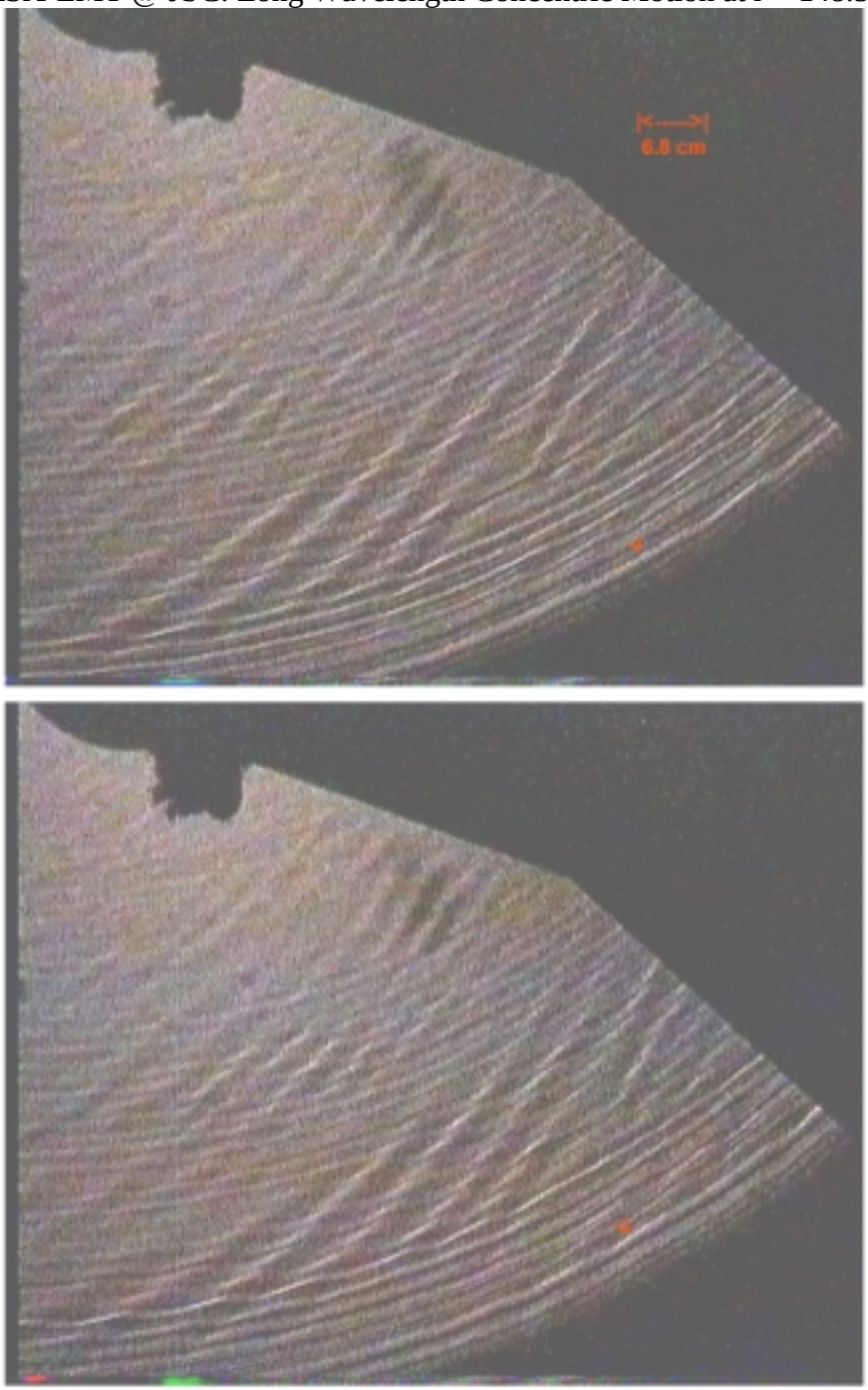

Figure IIIE.4-2. Two video frames of the NASA liquid mirror acquired under point-source illumination at the radius of curvature. The red arrows indicate two positions (r=148.5 and 146 cm) on a long wavelength concentric wave against which the wave motion was measured. The frames are separated by 0.067 seconds (2 video frames) in which time the concentric wave front moved radially inward 2.0 cm (1 wavelengths) implying a frequency of 15 Hz. (Rot: CCW)

NASA-LMT @ JSC: Long and Short Wavelength Concentric Waves

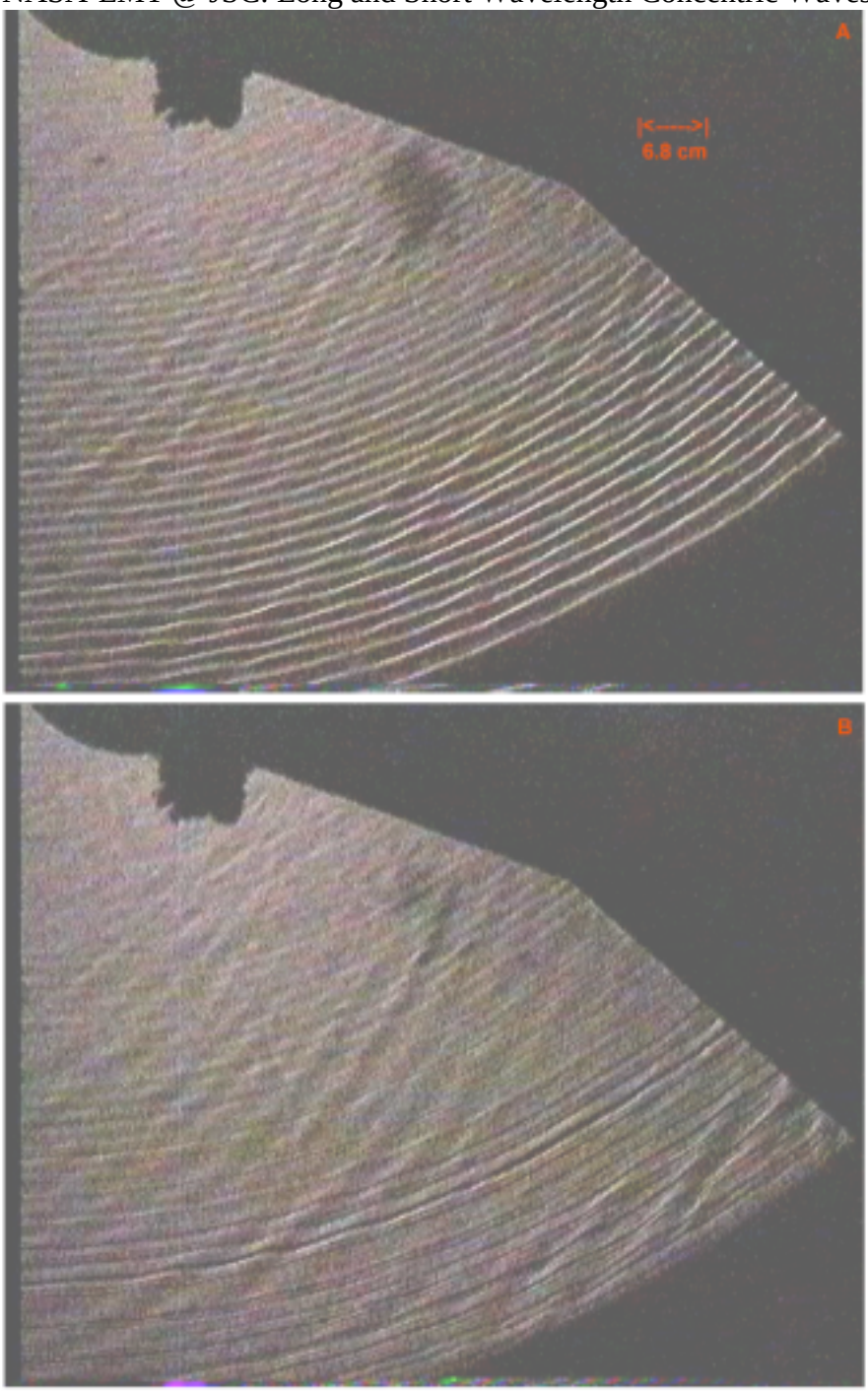

Figure III.E.4-3. An illustration of the two types of concentric waves observed at larger radii (r >75 cm) on the NASA-LMT. The upper frame shows the long wavelength concentric waves ($\lambda \cong 1.36$ to 1.7 cm; 52.5 Hz) and the lower frame shows the short wavelength concentric waves ($\lambda \cong 0.68$ cm; 21 Hz). Both images were extracted from video frames acquired under point-source illumination at the radius of curvature. (Rot: CCW)

NASA-LMT @ NODO: Region Surrounding the Mirror Central Hub

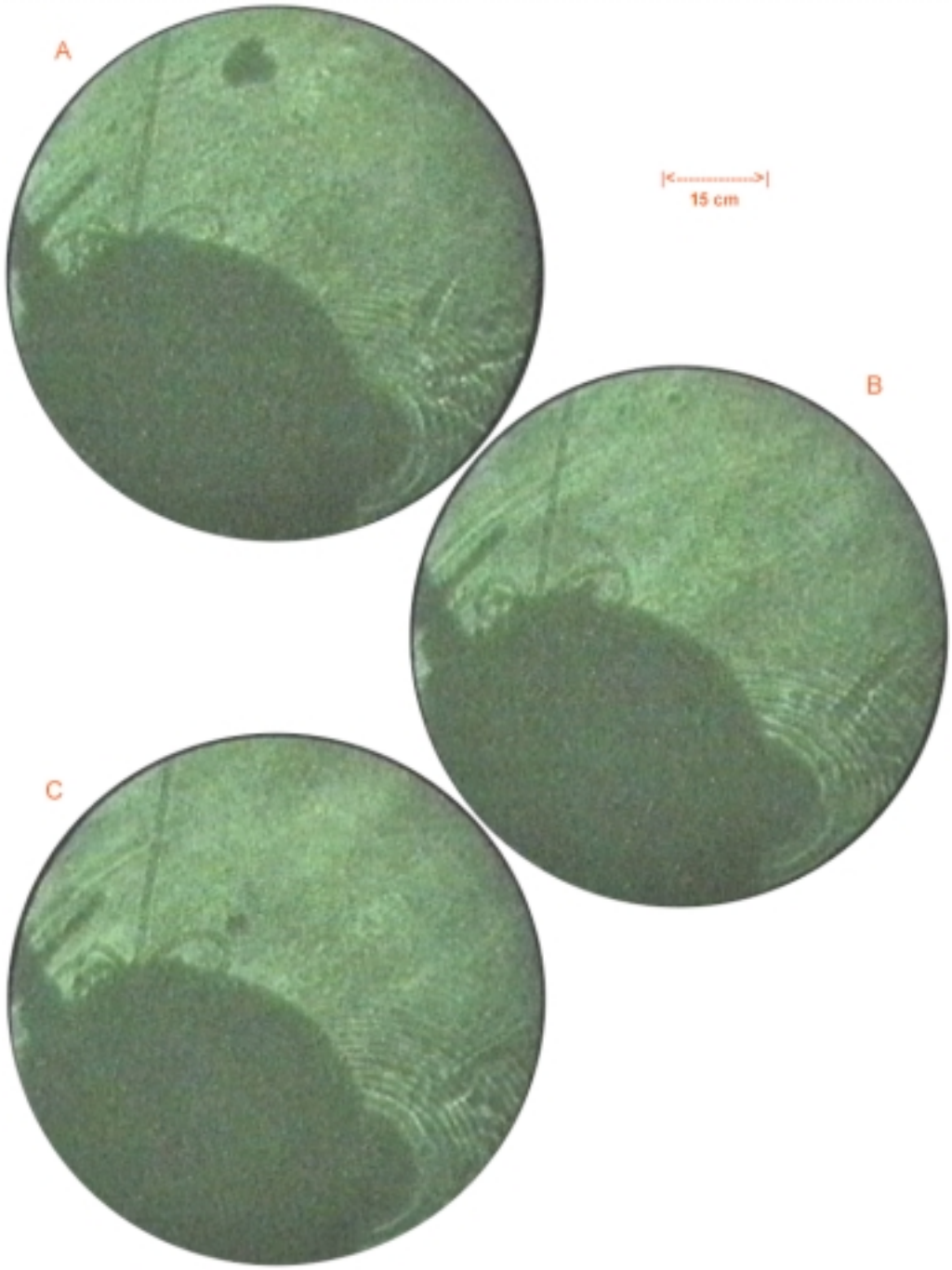

Figure III.E.4-4. Time series of images demonstrating concentric surface waves ($\lambda \cong 1.15$ to 1.7 cm) emanating from the mirror central hub. The region surrounding the mirror central hub is made visible by point source illumination from a bright off-axis star. The shadow of the prime focus (PF) assembly is also visible as well as waves of heated air streaming from the prime focus mounted CCD controller (radial streamers near hub). The large scale (~10 cm diameter) dark and light mottling over the mirror surface results from wave front errors induced by atmospheric seeing cells of diameter R_o. (Frames are separated by 0.3 seconds; Rotation: CW)

installation - perhaps due to the transmission of silo wind loads to the mirror pier through the ground or building footer. This idea is supported by laboratory notes indicating that the short wavelength waves were more prominent when the exterior winds were strong.

Long wavelength (LW) concentric waves ($1.15 < \lambda < 2.0$ cm) have been observed at both the JSC and NODO installations. These waves emanate from both the mirror perimeter and the central hub. They have a frequency of approximately 15 Hz and may possibly be stationary waves with zero group velocity. Measurements are not sufficiently accurate to make a definite determination however. They do not correlate well with either the Landau and Lifshitz or the Hickson dispersion relations, although for some wavelengths the frequency and phase velocity agree. The source of these waves is probably related to the natural oscillation frequency of the mirror container which Hickson (1993) has shown is 18 Hz for a 2.7 meter diameter mirror containing a 2mm Hg layer and 27 Hz for an empty container. The 3 m NASA mirror is of almost identical construction and probably has a comparable resonant frequency near 18 Hz with Hg layers of either 1.61 mm (NODO) or 2.25 mm (JSC). The postulate that mirror resonance is the source of the concentric waves is supported by the identical frequencies observed both at NODO and JSC despite significant differences in the mirror infrastructure and pier construction. The NODO pier, for example, has a natural resonant frequency of between 10 and 15 Hz (Hickson PC), whereas the JSC pier has a resonant frequency of greater than 1000 Hz. It is unlikely, however, that the NODO pier is the source of the concentric waves since the observed wave frequencies at NODO and JSC are identical within the limits of measurement.

The excitation of mirror oscillations could arise from several sources. It has been correlated with wind loading on the observatory structure via an increase in the amplitude and extent of the concentric waves during windy conditions at both NODO and JSC. The JSC observations were made with the observatory closed to preventing direct contact of moving air with the mirror which can create severe turbulence (as shown in Figure III.E.4-5). The NODO observations were also made with the observatory closed, but the waves were visible with the unaided eye on the mirror surface. Each exterior gust of wind generated concentric ripples visible at the mirror perimeter, despite the fact that no wind actually impacted the mirror surface. In both cases, the wind load on the facility is transmitted through the common ground between observatory and pier. Activities within the building itself can also induce mirror vibrations. At NODO, vibrations from the first floor mechanical room which contains ventilation systems, and a portion of the air bearing compressed air system, may be transmitted to the pier through the ground. The brush-less DC direct-drive motor which energizes each of 12 poles with a sinusoidal voltage at 2 Hz is another possible, though unlikely source of excitation. F-noise (1/f) in the bearing air film has been excluded as a source due to the small amplitude (A<5 nm; Dahl PC).

5) Transitory Waves – Impact Induced

The mirror is occasionally subject to impact from an insect or a piece of debris. If the mirror and Hg are in rotational equilibrium, this has the effect of creating a small

NASA-LMT @ JSC: Mirror Surface Turbulence

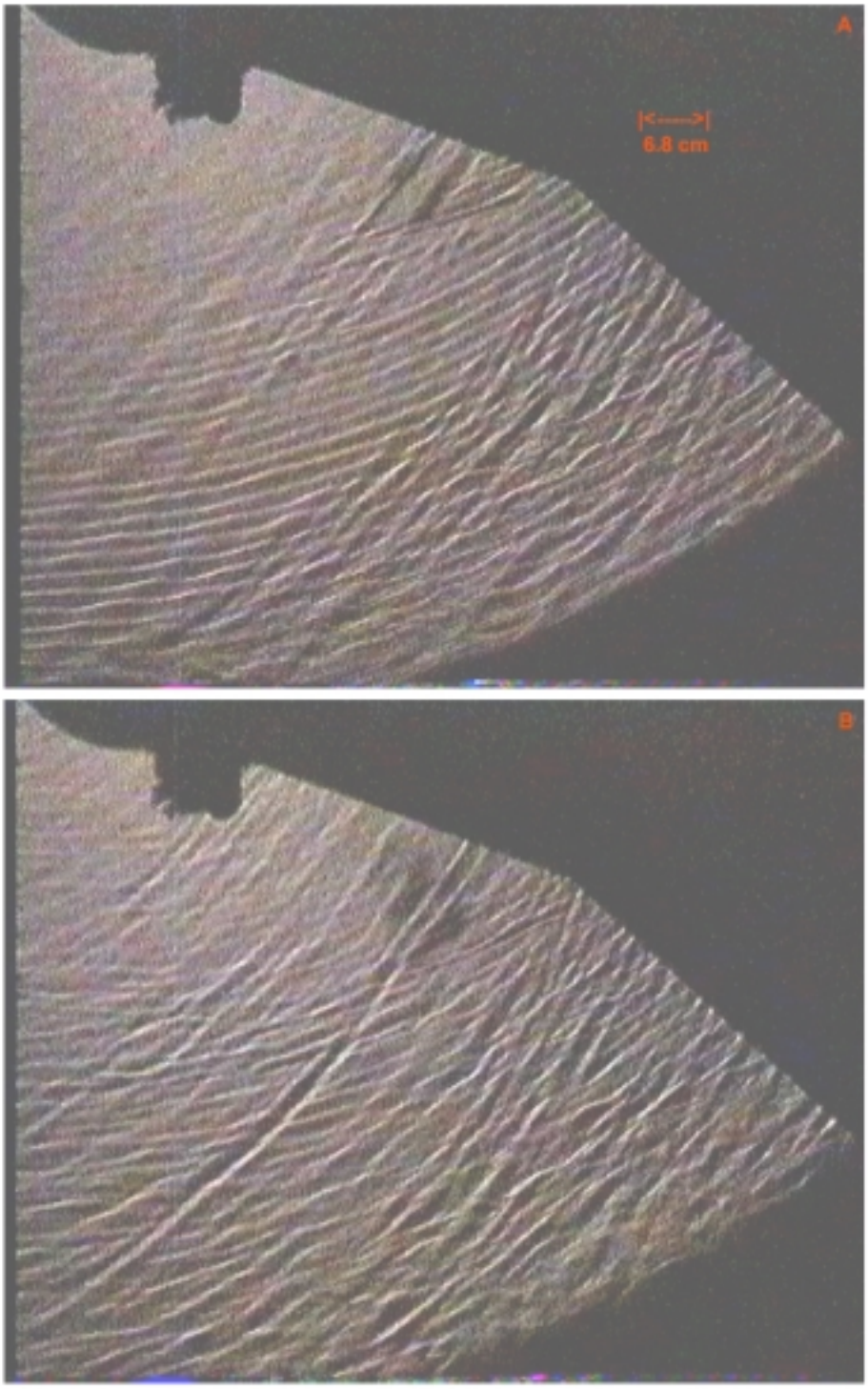

Figure III.E.4-5. Turbulence generated on the mirror Hg surface while impacted directly by a flow of air. This problem is easily mitigated by proper baffling and shielding of the primary mirror. (Rotation: CCW)

circular tear in the Hg surface which remains until the mirror is stopped and restarted. Since in equilibrium there is no flow of Hg relative to the mirror surface, the created hole has a stable size (usually < 1 cm diameter). If the impact occurs prior to mirror stabilization (Chapter IV), then the resultant tear in the Hg surface will grow rapidly in size and the mirror will need to be restarted before it becomes unbalanced. Figure III.E.5-1 shows the expansion of a circular wave-front on the NASA-LMT after a piece of debris has impacted the mirror and Table III.E.5-1 lists the parameters associated with this wave along with a comparison with the dispersion relation predictions. The observed group velocity matches the Landau and Lifshitz prediction with the caveat that the correlation could be coincidental since only a single series of measurements (limited to the wavelength and wave-front expansion velocity) were acquired.

Table III.E.5-1. Parameters for Impact Induced Expanding Wave Front

A	B	C	D	E	Landau and Lifshitz			Hickson		
$\lambda \pm 0.3$ cm $[k]$ (cm^{-1})	ν (Hz) $[\varpi]$ $\frac{rad}{\sec}$	V_G ± 3 $\frac{cm}{\sec}$	V_P $\frac{cm}{\sec}$	V ± 3 $\frac{cm}{\sec}$	$[\varpi_{LL}]$ $\frac{rad}{\sec}$	V_G $\frac{cm}{\sec}$	V_P $\frac{cm}{\sec}$	$[\varpi_H]$ $\frac{rad}{\sec}$	V_G $\frac{cm}{\sec}$	V_P $\frac{cm}{\sec}$
1.25 [5.03]	ID	ID	ID	20.0	[87.8]	21.3	17.5	[104]	30.4	20.6

NASA-LMT @ JSC: Post-impact Circular Wave Propagation

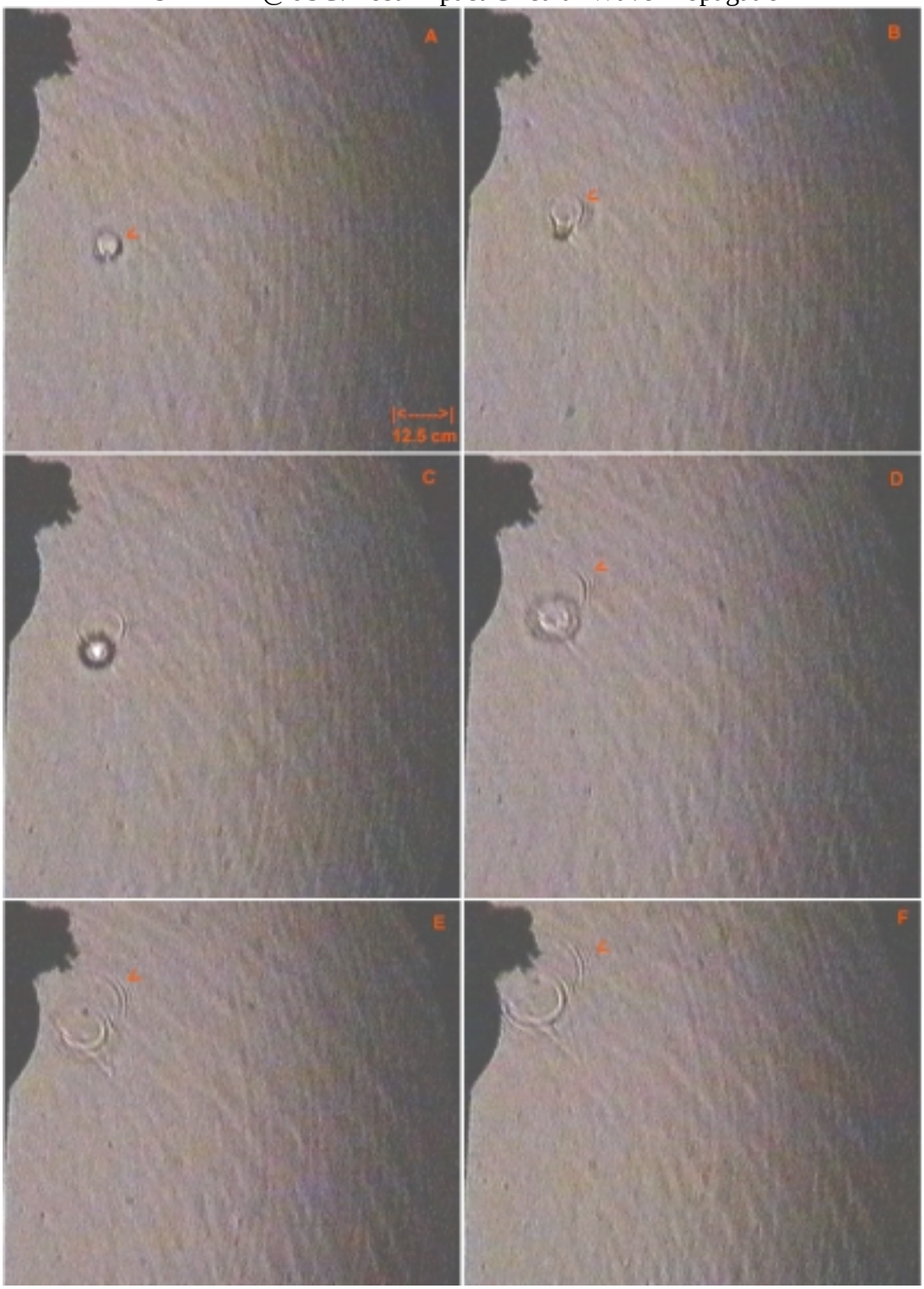

Figure III.E.5-1. Propagation of a wave resulting from an impact to the mirror by a piece of debris. The circular wave front has $\lambda \cong$ 1.25cm and moves radially outward at ~20 cm/sec. Frames are separated by 0.067 seconds. (Rotation: CCW)

6) Wave Damping –

Although it is difficult to eliminate waves on the surface of a liquid mirror, they can be partially mitigated by using thinner Hg layers. To see why this is true, we begin with the expression for the damping coefficient of a fluid wave (Landau and Lifshitz 1959):

$$WaveAmplitude = A = A_0 e^{-\gamma t} \qquad \text{(III.E.6a)}$$

Where:

Damping coefficient = $\gamma = 2 \cdot \nu \cdot k^2$

ν = kinematic viscosity (0.0012 $cm^2/\sec$ cm/sec for Hg)

k = wave number

The Hg layer thickness and wave number are related to each other and the angular wave frequency by the dispersion relation. If we hold the angular wave frequency constant in the Landau and Lifshitz dispersion relation (Equation III.E.1a), then as the Hg layer thickness (h) decreases, the wave number (k) must increase. As an example we consider the NASA-LMT with Hg layer thicknesses of 0.5, 1.0, 1.5, and 2.0 mm and a wave with a frequency of 15 Hz (at or near the mirror resonant frequency). Using the Landau and Lifshitz dispersion relation and solving numerically for k yields the damping coefficients shown in Table III.E.6-1.

Table III.E.6-1. Damping Coefficient and Hg Layer Thickness

Wave Frequency: 15 Hz (94.2 rad/s)	Mirror Hg Thickness h (mm) 0.5	1.0	1.5	2.0
$k(cm^{-1})$	7.73	6.41	5.80	5.44
$\lambda(cm)$	0.81	0.98	1.08	1.15
$\gamma = 2 \cdot \nu \cdot k^2$ ($\sec^{-1}$)	0.143	0.0986	0.0807	0.0710
t_c (sec)	7.0	10.1	12.4	14.1

It is apparent that the characteristic timescale for wave damping ($t_c = \gamma^{-1}$) decreases as roughly the square root of the layer thickness ($\sqrt{h}$) for constant frequency. Thus thinner layer will damp waves more effectively.

Using the Hickson dispersion relation (III.E.1d) we can demonstrate analytically the dependence of the damping coefficient on both Hg layer thickness and angular frequency. Using the quadratic formula to solve for wave number (k) and substituting into the expression for the damping coefficient, we obtain:

$$\gamma = 2 \cdot \nu \cdot k^2 = \frac{\nu\rho}{\alpha}\left[\sqrt{\frac{1}{h\rho}(4\alpha\varpi_H{}^2 - 16\alpha\Omega^2) + g^2} - g\right] \qquad \text{(III.E.6a)}$$

Thus for $\varpi_H{}^2 > 4\Omega^2$ (which is always true for waves observed on the NASA LMT), we

have wave damping with the damping coefficient increasing for both increasing angular wave frequency and for decreasing Hg layer thickness. As verification, this expression returns similar values to those listed in Table III.E.6-1.

Borra has emphasized repeatedly the importance of using thin Hg layers to mitigate the adverse effects of waves (Borra et al. 1992, Girard and Borra 1997). He has established layers as thin as 0.5 mm. At the NASA-LMT we operate with as thin a layer as possible (1.61 mm) before imperfections on the mirror container surface make establishing the Hg layer extremely difficult. Layers which are too thin can be subject to print-through wherein mirror container surface features become visible on the Hg upper surface. Hickson (PC) has shown that defects which protrude more than 10% into the Hg layer will be visible on the Hg surface. This may already be a problem at the NASA-LMT where spin-casting defects may be visible on the Hg surface as discussed in Chapter V.

It is important to note that because the mercury surface rapidly oxidizes (Chapter IV), the actual wave damping coefficients are greater (shorter damping timescales) than those derived here for an un-oxidized Hg surface. Since Tremblay and Borra (2000) have observed a dramatic increase in wave damping with moderate reductions in layer thickness, the trend toward greater damping with thinner layers may be enhanced by the oxide formation as the oxide's damping characteristics disproportionately dominate fluid thickness effects for progressively thinner layers.